Master's Thesis

Master's Degree in Quantum Science and Technology

Entanglement Properties and Dynamics of Collectively Dissipating Multilevel Atom Arrays

Guillem Lancis Beneyto

Supervisors: Maria Moreno Cardoner, Eric Sánchez Llorente

Departamet de Física Quàntica i Astrofísica, Universitat de Barcelona

Master in Quantum Science and Technology Barcelona

Universitat de Barcelona

Barcelona, September 2025

Entanglement Properties and Dynamics of Collectively Dissipating Multilevel Atom Arrays

Guillem Lancis Beneyto

Supervised by: Maria Moreno Cardoner, Eric Sánchez Llorente

Departament De Física Quàntica i Astrofísica, Universitat de Barcelona, Carrer de Martí i Franquès, 1, 11, Districte de Les Corts, 08028, Barcelona

24 August 2025

Achieving an efficient and controllable atom-light interface is essential for quantum technologies. In this context, subwavelegnth atomic arrays provide a promising platform, as collective radiance effects can be exploited to achieve an enhanced atom-light coupling and a higher fidelity in certain quantum optics protocols. In such systems, constructive (*superradiance*) and destructive (*subrradiance*) interference between the scattered photons enables to suppress spontaneous emission into undesired optical modes, while enhancing it into desired, detectable modes.

In this work, we explore how these ideas, originally developed for two-level atoms, can be extended to multilevel structures with a focus on Λ-type atoms with one excited state and two degenerate ground states. To this end, we generalize the open quantum spin model to multilevel atoms and apply it to Λ systems. We study the collective radiative properties and the entanglement of Dicke states, using a mapping onto $\mathrm{SU}(3)$ algebra. Furthermore, we analyse how finite-size effects and coherent interactions modify collective radiance, leading to the emergence of darker states in the two excitation manifold of Λ-systems, compared to the case of two-level atoms, for an atom number $N \geq 10$. We also study the dissipative Dicke dynamics for a fully inverted initial state, showing that the evolution is restricted to the symmetric sector. In the finite-size array case in presence of coherent interactions, we identify a peak in the dynamical evolution of entanglement, coinciding with the superradiant burst and find that the system reaches a non-trivial entangled steady state.

Keywords: Atomic arrays, multilevel atoms, Λ-atoms, collective radiance, superradiance, subradiance, open quantum spin model, Dicke model, $\mathrm{SU}(3)$, entanglement, negativity, open system dynamics, steady-state

Guillem Lancis Beneyto: guillemlancis@gmail.com

Acknowledgements

Despite being written by me, this Master's thesis could not have been possible without the help of many others.

Firstly, I would like to thank María Moreno for all her scientific advice, help and kindness during my final degree project and the writing of this thesis. I would also like to express my gratitude to Eric Sánchez, who joined this project without hesitation and enriched every discussion with his comments. It has been a pleasure!

I would also like to thank the entire ManboQu Group (Many-Body Quantum Physics with Atoms and Light) for the wonderful months during which I not only worked on this Master's thesis, but also enjoyed collaborating on other outreach projects.

Special thanks go to my office mates Marc Camus, Joan Ainaud and Miguel Carrasco (637k for fireman), who created a perfect work environment during these months. I am sure that everyone's Master's thesis has been influenced by each other's work. You all deserve the best in your next steps.

Finally, I would like to thank my family and closest friends for always supporting me. In particular, I would like to thank my parents and sister for their unconditional support, which I have always received without expectation of anything in return. This work also belongs to you.

Contents

List of Figures

1 Introduction

The progress of atomic physics has been closely linked to the development of new optical techniques. Atom–light interactions lie at the heart of fundamental processes such as the absorption and emission of radiation. Furthermore, the ability to manipulate the rich internal structure of atoms using electromagnetic fields has become an essential tool over the past decades for cooling and trapping techniques to access, control, and coherently manipulate atomic states with high precision [1, 2, 3]. This level of control has given atomic systems such as ultracold neutral atoms and trapped ions a central role in the development of quantum technologies [4], including quantum metrology [5], quantum information processing and communication [6], and the study of synthetic quantum matter [7]. In particular, structured arrays of ultracold atoms implemented using reconfigurable optical tweezers [8, 9, 10] or optical lattices [11] have emerged as versatile and scalable platforms for quantum computation [12] and quantum simulation [13], offering microscopic control over interactions and geometry that are hard to achieve in natural systems.

Beyond their computational capabilities, neutral atom arrays can be exploited as an efficient quantum optics platform when interfacing with light. This is crucial for a wide range of applications, including photon storage or quantum memories that are essential components in long-distance quantum communication [6], distributed quantum computing and networking [14]. Moreover, it provides a test-bed for fundamental studies on atom-light interactions at the quantum level, such as the generation of highly entangled states of atoms and photons and the emergence of exotic light properties [15].

Thus, achieving an efficient and controllable atom-light interface is essential for all the above mentioned tasks. However, in free space a single atom interacts only very weakly with a single photon [4]. This limitation arises because the optical field radiated by an atom through spontaneous emission does not match the spatial mode of a propagating field such as a laser beam. Instead, the atom emits photons into a broad distribution of optical modes, most of which cannot be collected. As a result, only a small fraction of the emitted light can be captured in the desired mode, leading to photon loss and, consequently, loss of information.

In experiments with large dilute atomic ensembles, spontaneous emission is usually considered an independent process for each atom, leading to an optical depth scaling linearly with the atom number N. The optical depth is the figure of merit in this context, proportional to $N(\lambda_0^2/A)$, where λ_0 is the transition wavelength and A the light beam area [4]. The quantity λ_0^2/A is the scattering cross section between a single atom and a single photon in free space, while the factor N reflects the assumption that each atom either succeeds or fails independently to scatter a photon. In diluted ensembles, the optical depth fundamentally bounds the minimum achievable error in protocols such as single-photon storage and retrieval [16] and spin squeezing [4], resulting in errors that can be suppressed at most as $1/N$.

As the interatomic distance decreases, the independent spontaneous emission assumption breaks down. In this regime, wave interference of the scattered fields by the atoms leads to collective interference effects in the emission process. Atoms couple through shared electromagnetic modes, leading to coherent dipole-dipole interactions and collective radiative effects. Depending on the symmetry of the collective atomic states, constructive interference can enhance photon emission, a phenomenon known as *superradiance*. Conversely, destructive interference can suppress the collective decay rate drastically leading to *subradiance*, and the formation of long-lived, decoherence-protected states.

These collective radiative phenomena were first described in the seminal work by Dicke [17], where atoms are confined within a volume much smaller than the wavelength of light, so that they couple to the same optical mode. This idealized model was later generalized by Lehmberg [18], who derived a full master-equation description of atoms at finite separations, revealing how dipole–dipole interactions and position-dependent decay rates govern cooperative effects. A comprehensive theoretical review, generalizing the phenomena beyond Dicke's model and providing connections with cavity quantum electrodynamics (cQED), was subsequently provided by Gross and Haroche [19]. Since then, such interactions have been extensively studied in the context of cQED, where atomic indistinguishability leads to analogous physics.

In this context, superradiance was first experimentally observed several decades ago in hot atomic

and molecular vapours within optical cavities [20, 21, 22]. It was later demonstrated in pairs of trapped ions and without a cavity [23]. More recently, superradiance has also been observed in artificial atoms in a cavity [24], in atomic ensembles coupled to nano-fibers [25, 26] or even in free space [27, 28, 29, 30]. In contrast, subradiance has remained experimentally elusive until recent years [23, 31, 32], largely due to its intrinsic decoupling from the electromagnetic field.

In recent years, these studies have been extended to ordered atomic arrays where particles are separated by subwavelength distances, where wave interference becomes maximal, in contrast to disordered atomic ensembles. In this regime, the full three-dimensional continuum of optical modes must be considered, and therefore interactions between atoms become position dependent. The broken permutational symmetry increases the complexity of the problem. Nevertheless, the spatial order in these systems reduces the dephasing effects, making atomic arrays a promising platform for studying many-body dissipative dynamics [33, 34].

Experimental advances using optical lattices [11], optical tweezers [8, 9, 10] and quantum gas microscopes [35, 36, 37] have demonstrated the ability to generate perfect one-, two- and three-dimensional atomic arrays. Furthermore, reconfigurable optical tweezers allow to create arbitrary geometries almost at will [9, 10]. Due to collective scattering of photons, the realization of atomically thin mirrors [38], as well as a single-atom photon switch [39], has been realized in this context. These platforms pave the way for the observation of other theoretical proposals in the field, such as photon storage with exponential improved fidelity using subradiant states [40, 41], coherent photon-photon gates [42], driven-dissipative phase transitions and phase separation [29, 43], quantum-enhanced sensing [44], and the engineering of entangled dark atomic states through the interplay of coherent driving and dissipation [45, 46].

While most theoretical studies have focused on two-level atoms with a single decay channel from the excited state to the ground state, real atomic systems exhibit intrinsically multilevel structures. Recent works already point out how these multilevel configurations can give rise to highly entangled subradiant and dark states [47, 48], how they also retain dynamical features like a superradiant burst [49], which can be used for ground state selection [50], and how it is possible the generation of highly entangled steady states using far-off resonant weak external fields [51, 52, 53]. However, a complete understanding of collective radiance in these more complex systems is still lacking. This Master's thesis aims to extend the study of collective radiance phenomena to multilevel atomic structures, where the competition between multiple decay channels can lead to novel and richer dynamical behaviour.

The manuscript is structured as follows. In Section 2 we introduce the physical system, together with a possible experimental implementation of this. In Section 3, the theoretical formalism describing quantum atom-light interactions and collective decay are introduced. The specific case of Λ-type atoms is considered, with a concrete description of the pure dissipative Dicke limit. In Section 4 we study the radiative and entanglement properties of the collective dissipative Dicke states, which can be well understood within the framework of the SU(3) group. The effect of finite size and coherent interactions are also studied. In Section 5 we analyse the dynamics of the Dicke model and the full model with finite size effects and coherent interactions with a fully inverted initial state. Finally, we look at the steady-state properties as a function of the inter-particle separation for the same model. In Section 6 we present our main conclusions and outlook directions for future work.

2 The system

In this section we introduce the model that will be studied in this thesis (Section 2.1) together with a potential physical implementation of this based on state-of-the art experiments (Section 2.2).

2.1 Multilevel Λ atomic structure

The system under study is depicted schematically in Fig. 1. It consists of N identical Λ-type atoms, each with an excited state $|e\rangle$ and two possible decay channels into degenerate ground states, $|g_1\rangle$ and $|g_2\rangle$. The photons emitted in the $|e\rangle \to |g_1\rangle$ and $|e\rangle \to |g_2\rangle$ transitions are circularly polarized, with polarization vectors: $\sigma^+ = \frac{1}{\sqrt{2}}(\hat{\mathbf{x}} + \mathrm{i}\hat{\mathbf{y}})$ and $\sigma^- = \frac{1}{\sqrt{2}}(\hat{\mathbf{x}} - \mathrm{i}\hat{\mathbf{y}})$. Both transitions are assumed to have the same wavelength λ_0 and be equally weighted, *i.e.* have the same dipole moment strength.

The atoms are trapped at fixed positions, *i.e.* we assume a deep trapping optical potential such as that provided by the optical tweezers. We consider two specific geometries: in the first configuration (left in Fig. 1), atoms are placed on a ring lying in the plane defined by the circularly polarized emission vectors $(\hat{\mathbf{x}} - \hat{\mathbf{y}})$, allowing us to study closed geometries where symmetry considerations can be exploited. In the other configuration (right in Fig. 1), atoms are arranged in a linear chain lying in the $\hat{\mathbf{x}}$ direction, enabling the study of simpler one-dimensional structures. When atoms are in the $\hat{\mathbf{x}} - \hat{\mathbf{y}}$ plane, the two transitions are no longer independent: photons emitted in a σ^+ transition can excite atoms in a σ^- transition, and viceversa. This happens because the emitted photons do not retain a uniform polarization within the plane of emission. Newer and interesting phenomena will happen when studying the mixing channels in contrast to the two-level case. In both cases, d is the distance between two adjacent atoms.

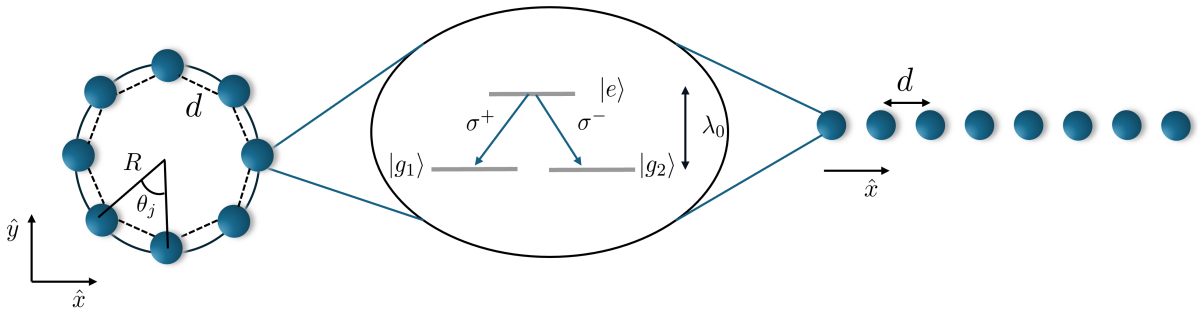

Figure 1: Schematics of the studied system. An ordered array of Λ atoms separated by distance d are dipole-dipole interacting. Two spatial configurations are considered: Geometrical configurations considered: a ring (left) and a linear chain (right) with N = 8 atoms. The ring lies in the $\hat{\mathbf{x}} - \hat{\mathbf{y}}$ plane, while the linear chain is aligned along $\hat{\mathbf{x}}$ axis. The inset describes Λ atomic level structure, consisting of two degenerate ground states $|g_1\rangle$ and $|g_2\rangle$ connected to the excited state $|e\rangle$ via orthogonal circularly polarized transitions σ^+ and σ^-.

2.2 Experimental implementation

Following the discussion in [49, 54, 55] alkaline-earth(-like) atoms (AEAs) provide a promising platform for realizing atomic arrays in the sub-wavelength regime, enabling the study of dissipative quantum optics in many-body systems. Their main advantage comes from their multiple allowed transitions: short-wavelength transitions allow for efficient cooling and trapping, while much longer-wavelength transitions are suitable for the quantum optics experiments.

As a concrete example, one can consider the atomic structure of bosonic species like ^{174}Yb or ^{88}Sr with two valance electrons. In these elements the nuclear spin is zero , $\mathrm{I}_{\mathrm{nuclei}} = 0$, meaning that no hyperfine structure needs to be taken into account (see Fig. 2(a)). The ground state $^1\mathrm{S}_0$ and metastable states $^3\mathrm{P}_{0,1,2}$ can be trapped using optical wavelengths. Exciting the atoms into $^3\mathrm{D}_{0,1,2}$ manifold enables decays to happen at infrared wavelengths, allowing for sub-wavelength interatomic spacing. In particular, ^{174}Yb shows greater interest, because the $^3\mathrm{D}_1 \to {}^3\mathrm{P}_1$ transition occurs at $1.540\mu m$, making it compatible

with telecommunication resources. On the other hand, for ^{88}Sr, $^3\mathrm{D}_1 \rightarrow {}^3\mathrm{P}_1$ transition occurs at the mid-infrared $2.9\mu m$, making it less compatible with experimental apparatus. For this reason, we will consider ^{174}Yb.

We study the decay of initial atoms prepared in the $|^3\mathrm{D}_1, m_J = 0\rangle$ state into $|^3\mathrm{P}_1, m_J = -1\rangle$ and $|^3\mathrm{P}_1, m_J = +1\rangle$ states via circularly polarized photons (σ^+ and σ^-, respectively). Several points must be taken into account to achieve this closed configuration:

1. The $|^3\mathrm{D}_1, m_J = 0\rangle \rightarrow |^3\mathrm{P}_1, m_J = 0\rangle$ transition is forbidden by the corresponding Clebsch-Gordan coefficient $\langle J_g = 1, m_g = 0; J_q = 1, q = 0 | J_e = 1, m_e = 0\rangle = 0$, being q the angular momentum of emitted photon in the given transition.

2. The $^3\mathrm{D}_1 \rightarrow {}^3\mathrm{P}_2$ decay has a strongly reduced linewitdh, with a branching ratio of $0.03 : 1$ [56] compared to $^3\mathrm{D}_1 \rightarrow {}^3\mathrm{P}_1$, and can be neglected.

3. $^3\mathrm{P}_1 \rightarrow {}^1\mathrm{S}_0$ at $556nm$, is too short in wavelength to be collectively enhanced. Moreover, its relatively slow rate does not allow for the observation of collective effects on experimentally relevant timescales.

4. Besides this, the $^3\mathrm{D}_1 \rightarrow {}^3\mathrm{P}_0$ transition has a non-negligible decay rate with a linearly polarized emitted photon (see Fig. 2 (b)). However, this photon is polarized in the perpendicular direction to the circularly polarized σ^+ and σ^- emitted photons.

As a starting point, we have studied perfect Λ-systems. However, all simulations presented in this work allow for a next-step generalization where the π-transition would be included, increasing the complexity of the Hilbert space. Other demanding experimental techniques such as repumping from $|^3\mathrm{P}_0, m_J = 0\rangle$ into the original $^3\mathrm{D}_1$ state can be thought to eliminate the π-transition and achieve the perfect Λ-system.

Taking these considerations into account, we can study the closed Λ-type configuration with the following states: $|e\rangle \equiv |^3\mathrm{D}_1, m_J = 0\rangle$, $|g_1\rangle \equiv |^3\mathrm{P}_1, m_J = -1\rangle$ and $|g_2\rangle \equiv |^3\mathrm{P}_1, m_J = +1\rangle$ (see Fig. 2 (b)). In order to confirm that the two branching ratios are equal, the Clebsch–Gordan coefficients for both transitions must be calculated: $\langle J_g = 1, m_g = \pm 1; J_q = 1, q = \mp 1 | J_e = 1, m_e = 0\rangle = \pm 1/\sqrt{2}$, where q is the photon angular momentum. Therefore, the total spontaneous decay rate is given by: $\Gamma_{\text{total}} = \Gamma_0^{g_1} + \Gamma_0^{g_2} = \omega_0^3/(3\pi\epsilon_0\hbar c^3)\,(1/2 + 1/2)\,|\wp|^2 = 2\Gamma_0$. Here, $\Gamma_0 = \omega_0^3|\wp|^2/6\pi\epsilon_0\hbar c^3$ is the decay ratio into each channel. As both transitions have identical decay rates, this system is an ideal platform for studying competition between decay channels. This is in contrast to schemes where one channel dominates and enables ground state selection dynamics.

3 Theoretical Framework

In this section, we present a theoretical framework for photon-mediated interactions in atomic arrays. We then particularize to atoms with a Λ-type level structure in free space (Section 3.3) and later derive expressions for the Dicke limit, in which all atoms are assumed to be in the same spatial location (Section 3.4)

3.1 Input-Output equation

When two atoms couple to the same radiation mode, this can lead to an exchange of virtual photons, resulting in coherent dipole-dipole interactions between the atoms. In addition, collective spontaneous emission of photons (collective radiance) can occur, where photons are emitted at a faster (superradinace) or reduced (subradiane) rate.

The standard quantized description of the electromagnetic field in free space involves an infinite number of bosonic modes in this problem, each of which is associated with creation and annihilation operators. To gain intuition on how atoms couple to radiation in the quantum regime, it is useful first to consider a classical analogy, where atoms can be regarded as oscillating electric dipoles.

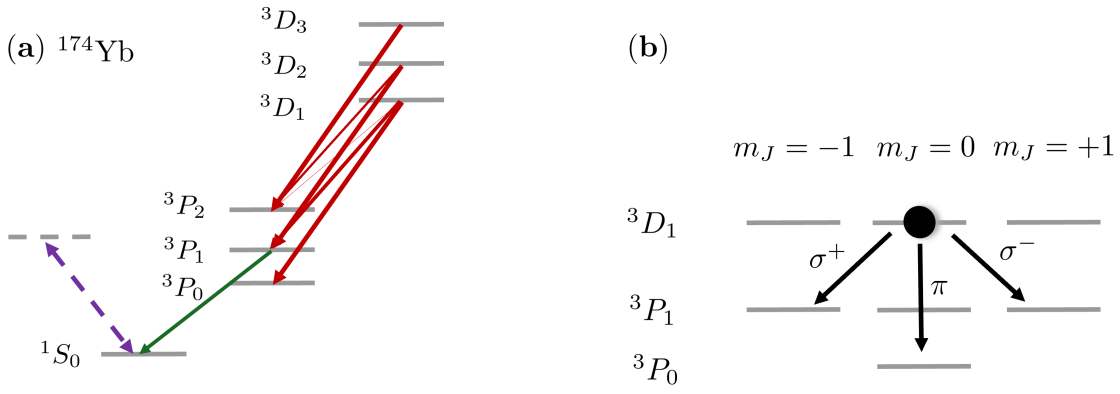

Figure 2: **(a)** Relevant atomic structure of ^{174}Yb. Violet dashed line indicate short wavelength optical trapping transitions. Solid lines correspond to possible decay channels, with line thickness proportional to the transition rate [57]. **(b)** Atoms are initially prepared in $|^3\mathrm{D}_1, m_J = 0\rangle$ and decay into $|^3\mathrm{P}_1, m_J = -1\rangle$ and $|^3\mathrm{P}_1, m_J = +1\rangle$ with circularly polarized emitted photons σ^+ and σ^-, respectively. Note the transition between $|^3\mathrm{D}_1, m_J = 0\rangle$ and $|^3\mathrm{P}_1, m_J = 0\rangle$ is forbidden. In principle, they can also decay into $|^3P_0, m_J = 0\rangle$ with linearly polarized emitted photons π. We will not consider this transition in our work.

Consider N classical electric dipoles $\mathbf{p}_i$ located at positions $\mathbf{r}_i$, driven by a monochromatic external field of frequency ω $\mathbf{E}_{\text{in}}(\mathbf{r}, \omega)$. The total electric field at any point is given by: $\mathbf{E}_{\text{out}}(\mathbf{r}, \omega) = \mathbf{E}_{\text{in}}(\mathbf{r}, \omega) + \sum_i \mu_0 \omega^2 \mathbf{G}(\mathbf{r} - \mathbf{r}_i, \omega) \cdot \mathbf{p}_i$, where $\mathbf{G}$ is the electromagnetic Green's tensor. The components of this tensor, $\mathbf{G}_{\alpha,\beta}$, with $\alpha, \beta \in \{x, y, z\}$ represent the α component of the electric field, generated by a dipole oriented along β direction. The Green's tensor is thus the solution to Maxwell's equations with a dipole point source and describes how the electromagnetic field propagates between two atoms. Because the fields obey a linear wave equation, interference between the scattered fields are inherently encoded in this tensor. This allows the description of light-mediated dipole-dipole interactions and collective radiance. This description holds in any linear, isotropic and dielectric media with the appropriate Green's function. In the case of free space, the Green's tensor between two atoms located at $\mathbf{r}_i$ and $\mathbf{r}_j$ is given by:

$$\mathbf{G}(\mathbf{r} = \mathbf{r}_i - \mathbf{r}_j, \omega_0) = \frac{e^{ik_0 r}}{4\pi k_0^2 r^3} \left[\left(k_0^2 r^2 + i k_0 r - 1 \right) \mathbf{1} + \left(-k_0^2 r^2 - 3 i k_0 r + 3 \right) \frac{\mathbf{r} \otimes \mathbf{r}}{r^2} \right], \tag{1}$$

where $k_0 = \omega_0 / c$ is the wave number of the atomic transition and $\mathbf{1}$ the identity 3×3 matrix.

The quantum fields also satisfy Maxwell's equations, and thus, it can be proven [40] that this equation still holds for the quantum case, when replacing the classical dipole moments by the electric dipole moment operators $\hat{\mathbf{p}} = -e\hat{\mathbf{r}}$ of the atoms, and the classical field by the quantum electric field operator $\hat{\mathbf{E}}(\mathbf{r}, \omega) = \hat{\mathbf{E}}^+(\mathbf{r}, \omega) + \hat{\mathbf{E}}^-(\mathbf{r}, \omega)$ (decomposed into its positive and negative frequency components). For two-level atoms, with ground $|g\rangle$ and excited $|e\rangle$ energy levels, the electric dipole moment operator associated with atom i can be written as $\hat{\mathbf{p}}_i = \wp^* \hat{\sigma}_i^{eg} + \wp \hat{\sigma}_i^{ge}$, with $\wp = \langle e | \hat{\mathbf{p}} | g \rangle$ the dipole moment matrix element. The input-output [58] equation for the (positive-frequency component) field reads:

$$\mathbf{E}^+_{\text{out}}(\mathbf{r}, \omega) = \mathbf{E}^+_{\text{in}}(\mathbf{r}, \omega) + \mu_0 \omega^2 \sum_i \mathbf{G}(\mathbf{r} - \mathbf{r}_i, \omega) \cdot \wp \hat{\sigma}_i^{ge}. \tag{2}$$

The above formalism can be readily generalized to the multilevel case as follows. Let us consider transitions between two fine levels J_g and J_e, more precisely, between the corresponding Zeeman sublevels denoted by the quantum numbers $m_g \in \{-J_g, \cdots, J_g\}$ and $m_e \in \{-J_e, \cdots, J_e\}$. The electric dipole moment operator can be written in this basis as

$$\hat{\mathbf{p}}_i = \sum_{m_g, m_e} \langle J_e m_e | \hat{\mathbf{p}} | J_g m_g \rangle \hat{\sigma}_i^{m_e m_g} + \text{h.c.} \tag{3}$$

Using the Wigner-Eckart theorem, we can rewrite the matrix elements in terms of the Clebsch-Gordan coefficients $C^q_{m_g}$:

$$\langle J_e m_e|\,\hat{\mathbf{p}}\,|J_g m_g\rangle = \frac{\wp}{\sqrt{2J_e+1}} C^q_{m_g} = (-1)^{J_e-m_e}\wp \begin{pmatrix} J_e & 1 & J_g \\ -m_e & q & m_g \end{pmatrix}, \tag{4}$$

where we have denoted by $\wp = \langle J_e\|-e\hat{r}\|J_g\rangle$ the reduced matrix element associated with the transition, and the matrix represents the $3-j$ symbols. Recall that q is the angular momentum of the emitted photon.

Note that the last expression always vanishes unless $m_e = m_g + q$ (i.e., electric dipole selection rules). We then can define the multilevel lowering operator for the allowed transitions as:

$$\hat{\Sigma}_{iq} = \sum_{m_g} C^q_{m_g}\hat{\sigma}_i^{m_g,m_g+q}, \tag{5}$$

and the corresponding raising operator as $\hat{\Sigma}^\dagger_{iq} \equiv \left(\hat{\Sigma}_{iq}\right)^\dagger$. The excitation number operator is also given by the sum over all possible photon polarizations $\hat{\sigma}_i^{ee} = \sum_{q\in\{0,\pm1\}} \hat{\Sigma}^\dagger_{iq}\hat{\Sigma}_{iq}$. Using these definitions, the input-output equation generalizes into:

$$\mathbf{E}^+_{\text{out}}(\mathbf{r},\omega) = \mathbf{E}^+_{\text{in}}(\mathbf{r},\omega) + \mu_0\omega^2\wp\sum_i \mathbf{G}(\mathbf{r}-\mathbf{r}_i,\omega)\cdot(\hat{\mathbf{e}}^q)\,\hat{\Sigma}_{iq}, \tag{6}$$

where now $\hat{\mathbf{e}}^q$ are the spherical basis vectors π, σ^+ and σ^- ($q\in\{0,\pm1\}$) as defined in Section 2.1.

3.2 Lindbladian and Open Quantum Spin Model

The atomic electric dipole moment operators are driven by the total fields at their positions, and at the same time, the fields depend on the atomic coherences, as we have seen in the previous equation Eq. (6). Starting from the electric dipole interaction Hamiltonian $\hat{\mathcal{H}} = -e\sum_i \hat{\mathbf{p}}_i\cdot\hat{\mathbf{E}}_{\text{out}}(\mathbf{r}_i,\omega_0)$ it is possible to derive, after tracing out the photonic degrees of freedom and in the Born-Markov and rotating wave approximations, a Lindblad master equation for the reduced atomic density matrix ρ. The Born-Markov and rotating wave approximations are well established in quantum optical systems [59]. In the Born approximation the coupling to the bath is assumed to be weak (only second order in perturbation theory), while in the Markov approximation the photonic bath is assumed to be memoryless or with very short correlation time compared to the atomic scale, what allows to obtain a master equation which is local in time and of the general form:

$$\dot{\rho} = -\frac{i}{\hbar}\left[\mathcal{H},\rho\right] + \mathcal{L}\left[\rho\right], \tag{7}$$

where $\mathcal{H}$ denoted the Hamiltonian part governing the coherent unitary evolution, and $\mathcal{L}$ corresponds to the Lindblad dissipator, describing the dissipation due to the coupling with the external bath.

In the case under study, of an array of multilevel atoms in free space and interacting with the electromagnetic vacuum, the Born-Markov approximation is equivalent to neglect light retardation, an assumption that is always valid for typical atomic cloud sizes, and to assume that the Green's function propagator varies only smoothly around the atomic transition frequency compared to the atomic absorption profile.

In this case, the operators $\mathcal{H}$ and $\mathcal{L}$ take the specific forms derived in [48, 54], that will be described next. The Hamiltonian $\mathcal{H}$ contains both the bare energy of the atoms and the coherent dipole-dipole interactions induced by the exchange of a virtual photon (from now on and for simplicity in the notation, we will set $\hbar = 1$):

$$\mathcal{H} = \omega_0\sum_i^N \hat{\sigma}_i^{ee} + \sum_{q,q'\in\{0,\pm1\}}\sum_{i,j}^N J_{ij}^{qq'}\hat{\Sigma}^\dagger_{iq}\hat{\Sigma}_{jq'}. \tag{8}$$

The Lindblad dissipator containing two types of terms (population recycling term and decoherence contributions), can be written as:

$$\mathcal{L}[\rho] = \frac{1}{2} \sum_{q,q' \in \{0,\pm 1\}} \sum_{i,j}^{N} \Gamma_{ij}^{qq'} \left(2\hat{\Sigma}_{jq'} \rho \hat{\Sigma}_{iq}^{\dagger} - \{\hat{\Sigma}_{iq}^{\dagger} \hat{\Sigma}_{jq'}, \rho\} \right). \tag{9}$$

The dissipative and dispersive couplings, $\Gamma_{ij}^{qq'}$ and $J_{ij}^{qq'}$, depend on how light propagates between the two quantum emitters, and are given by the real and imaginary parts of the Green's tensor, respectively:

$$\Gamma_{ij}^{qq'} = \frac{\mu_0 \omega_0^2 |\wp|^2}{2} (\hat{\mathbf{e}}^q)^* \cdot \mathrm{Im}\left[\mathbf{G}\left(\mathbf{r}_i - \mathbf{r}_j, \omega_0\right)\right] \cdot \hat{\mathbf{e}}^{q'} \tag{10a}$$

$$J_{ij}^{qq'} = -\mu_0 \omega_0^2 |\wp|^2 (\hat{\mathbf{e}}^q)^* \cdot \mathrm{Re}\left[\mathbf{G}\left(\mathbf{r}_i - \mathbf{r}_j, \omega_0\right)\right] \cdot \hat{\mathbf{e}}^{q'}. \tag{10b}$$

Note that these operators, in principle, account for processes where an atom emitting a photon with polarization q can induce absorption in another atom with a different polarization $q' \neq q$. This reflects the fact that the electromagnetic field generated by a dipole oriented along a given direction generally contains orthogonal components. The exact strength of this coupling, and the fact that it vanishes or not, are determined by the Green's tensor propagator.

The dynamics under Eq. (7) can be analogously described by the quantum jump formalism of open quantum systems (see Appendix A). In this picture, the system evolves deterministically under an effective non-hermitian Hamiltonian $\mathcal{H} = \omega_0 \sum_i^N \hat{\sigma}_i^{ee} + \mathcal{H}_{\text{eff}}$ interrupted by stochastic quantum jumps. The effective Hamiltonian reads:

$$\mathcal{H}_{\text{eff}} = \sum_{qq' \in \{0,\pm 1\}} \sum_{i,j}^{N} \left(J_{ij}^{qq'} - i \frac{\Gamma_{ij}^{qq'}}{2} \right) \hat{\Sigma}_{iq}^{\dagger} \hat{\Sigma}_{jq'}, \tag{11}$$

and leads to the deterministic part of the evolution given by $\mathcal{K}[\rho] = -i\,[\mathcal{H}_{\text{eff}}, \rho]$. This Hamiltonian has the form of a generalized *open quantum spin model*, where the raising and lowering operators $\hat{\Sigma}_{iq}^{(\dagger)}$ play the role of generalized spin operators, and the couplings are complex-valued.

On the other hand, jumps or decays are encoded in the jump superoperator

$$\mathcal{J}[\rho] = \sum_{qq' \in \{0,\pm 1\}} \sum_{i,j}^{N} \Gamma_{ij}^{qq'} \hat{\Sigma}_{jq'} \rho \hat{\Sigma}_{iq}^{\dagger}. \tag{12}$$

The total dynamical evolution is described by the Liouvillian superoperator, being the sum of the two different terms described before: $\mathcal{O} = \mathcal{K} + \mathcal{J}$.

From this, the transition rate between two different collective eigenstates of the effective Hamiltonian, $|\psi_{\xi}^{n_{ex}}\rangle$ with n_{ex} excitations and $|\psi_{\xi'}^{n_{ex}-1}\rangle$ with $n_{ex} - 1$ excitations, is given by:

$$\gamma_{\xi,\xi'} = \mathrm{Tr}\left(|\psi_{\xi'}^{n_{ex}-1}\rangle\langle\psi_{\xi'}^{n_{ex}-1}| \mathcal{J}\left[|\psi_{\xi}^{n_{ex}}\rangle\langle\psi_{\xi}^{n_{ex}}| \right] \right). \tag{13}$$

Another important parameter is the photon emission rate by the atomic array. To quantify it, we can use the rate at which the excited-state population decreases, *i.e.*, how quickly atoms decay to the ground state while emitting photons. At any time during the dynamical evolution, it can be calculated as:

$$R(t) = -\frac{d}{dt} \sum_i \langle \hat{\sigma}_i^{ee} \rangle, \tag{14}$$

where $\hat{\sigma}_i^{ee}$ is the excited-state number operator of atom i and the expectation value is taken over the atomic reduced density matrix at time t. The photon emission rate $R(t)$ is proportional to the light emitted power of the array, since multiplying it by the photon energy $\hbar\omega_0$ gives the total radiated power, *i.e.* energy per unit of time.

3.3 Λ Atoms

As discussed in Section 2.2, in this work we will consider three-level Λ-type atoms, with only two possible decay channels. In this case, the Clebsch-Gordan coefficients for both decay channels are equal, and the generalizing lowering and rising operators contain a single operator:

$$\hat{\Sigma}_{i,q=+1} \equiv \hat{\sigma}_i^{g_1 e}, \quad \hat{\Sigma}_{i,q=-1} \equiv \hat{\sigma}_i^{g_2 e}. \tag{15}$$

For this simpler case, the Fig. 3 shows the dependence on both dissipative and dispersive couplings as a function of the normalized interparticle distance d/λ_0 with two atoms separated along $\hat{\mathbf{x}}$ axis. Panel (a) shows the normalized dissipative coupling Γ_{ij}^{qq} (green) and $\Gamma_{ij}^{qq'}$ (red), corresponding to decay through the same or different ground states respectively. Panel (b) show the corresponding dispersive couplings J_{ij}^{qq} (green) and $J_{ij}^{qq'}$ (red), again same channel and mixed channel interactions. In all plots it can be seen that in the dilute limit $d/\lambda_0 \gg 1$, couplings between different atoms vanish and atoms behave independently, with a decay rate $\Gamma_0 = \Gamma_{ii}^{qq}$ for each decay channel q (note that $\Gamma_{ii}^{qq'} = 0$). In this case, the computational basis is enough to describe the physics and no collective phenomena is described. For shorter distances $d/\lambda_0 \sim 1$ collective effects begin to emerge, and for $d/\lambda_0 \ll 1$, the system enters the Dicke regime, where all atoms couple to the same electromagnetic field strength, and the Hamiltonian greatly simplifies (see Section 3.4). In this case a collective basis is needed to describe the problem as will be discussed later.

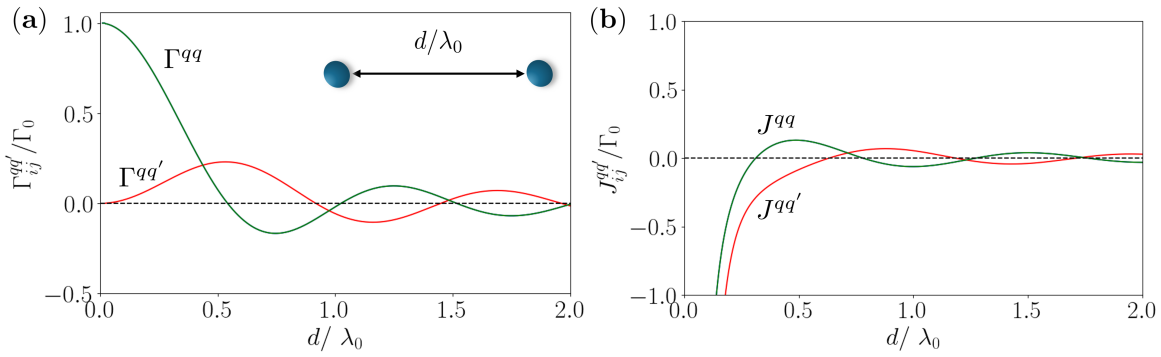

Figure 3: **(a)** Dissipative coupling $\Gamma_{ij}^{qq'}$ and **(b)** dispersive coupling $J_{ij}^{qq'}$ between two atoms, normalized to the single channel decay rate Γ_0, as a function of the normalized interatomic distance d/λ_0. In both panels, green lines represent couplings involving the same transition in the two atoms, whereas red lines correspond to the crossed terms.

3.4 Point-like atomic gas: the Dicke limit

As a starting point for our studies, we will focus on the dissipative Dicke regime [17], where all atoms are assumed to be confined at a very small volume (point-like gas limit) and only dissipative couplings are present. In this case, all the non-vanishing couplings $\Gamma_{ij}^{qq'}$ (including self-interacting terms) take the same value, thus greatly simplifying the model and leading to a permutationally symmetric Hamiltonian. This model captures essential physics relevant to some experimental platforms like atoms coupled resonantly to an optical cavity in the so-called bad cavity regime (cavity loss dominated over reabsorption) or atoms coupled to a waveguide and separated by a distance λ_0. In all these scenarios, the atoms are indistinguishable from the field's perspective, and collective eigenstates (rather than product states in the computational basis) become the natural basis.

More precisely, the Dicke regime corresponds to $d/\lambda_0 \to 0$, where all particles are coupled to the same amplitude of the electromagnetic field. The dissipative couplings become diagonal $\mathrm{Im}\left[\mathbf{G}(\mathbf{r_i} - \mathbf{r_j}, \omega_0)\right] \propto \mathbf{1}$, thus leading to $\Gamma_{ij}^{qq'} = \Gamma_0 \delta_{qq'}$, for any i and j (see Fig. 3(a)). Moreover, also strictly in this limit,

and following a regularization procedure [60], it can be seen that the dispersive part of the interactions $\mathrm{Re}\left[\mathbf{G}(\mathbf{r_i}-\mathbf{r_j},\omega_0)\right] \propto \mathbf{1}$ is also proportional to the identity, thus not changing the structure of the effective Hamiltonian $\mathcal{H}_{\text{eff}}$. As we are interested in the dissipative properties, and the collective eigenmodes are the same, we will work for convenience with the Hamiltonian that results from setting $J_{ij}^{qq'}=0$.

Therefore, in this limit we are left with the following permutationally invariant operators:

$$\mathcal{H}_{\text{eff}} = -i\frac{\Gamma_0}{2}\sum_{ij}(\hat{\sigma}_i^{eg_1}\hat{\sigma}_j^{g_1e}+\hat{\sigma}_i^{eg_2}\hat{\sigma}_j^{g_2e}) \tag{16a}$$

$$\mathcal{J}\left[\rho\right] = \Gamma_0\sum_{ij}\left(\hat{\sigma}_i^{g_1e}\rho\hat{\sigma}_j^{eg_1}+\hat{\sigma}_i^{g_2e}\rho\hat{\sigma}_j^{eg_2}\right). \tag{16b}$$

In the next Section 4, Eq. (16a) and Eq. (16b) will be used to classify and obtain the properties of the collective eigenstates in the Dicke limit.

4 Collectively Radiant Eigenmodes

In this section we study the collective eigenmodes of the system defined as the eigenstates of the effective Hamiltonian $\mathcal{H}_{\text{eff}}$, which as previously discussed, describes the deterministic evolution of the system. We begin by characterizing the dissipative Dicke eigenstates for two-level atoms (Section 4.1.1), and then extend the discussion to our proposal for Λ-type atoms, which can be mapped into SU(3) (Section 4.1.2)). An entanglement characterization of Dicke eigenstates is also included (Section 4.1.3). In Section 4.2, the collective eigenstates described before are used to solve the problem with finite interparticle distance and adding dispersion.

4.1 Dissipative Dicke model

For independent spontaneous emission ($d/\lambda_0 \gg 1$), the computational basis diagonalizes the Hamiltonian. In contrast, correlated spontaneous emission requires a collective basis reflecting interference effects. To understand cooperative emission, it is instructive to analyse first the dissipative Dicke states obtained in the limit of $d/\lambda_0 \to 0$. Dicke states already encode the essential collective radiative properties that are the key point of our work.

4.1.1 2-level atoms: SU(2) mapping.

To gain some intuition, we start describing the case of two-level atoms. These can be described as spin-1/2 particles, with $|g\rangle \equiv |\downarrow\rangle$ and $|e\rangle \equiv |\uparrow\rangle$ levels. In this case, the effective Hamiltonian reads:

$$\mathcal{H}_{\text{eff}} = -i\frac{\Gamma_0}{2}\sum_{ij}^{N}\hat{\sigma}_i^{eg}\hat{\sigma}_j^{ge} = -i\frac{\Gamma_0}{2}S^+S^- = -i\frac{\Gamma_0}{2}\left(\mathbf{S}^2-S_z^2+S_z\right), \tag{17}$$

where the collective raising and lowering spin operators are defined respectively as $S^+=\sum_{i=1}^N\hat{\sigma}_i^{eg}$ and $S^-=\sum_{i=1}^N\hat{\sigma}_i^{ge}$, while the total spin operator and its projection along z-axis are $\mathbf{S}^2=(S^+S^-+S^-S^+)/2+S_z^2$ and $S_z=\sum_{i=1}^N(\hat{\sigma}_i^{ee}-\hat{\sigma}_i^{gg})/2$. Since $[\mathcal{H}_{\text{eff}},S_z]=0$, the Hamiltonian in Eq. (17) can be diagonalized in blocks with fixed excitation number. The collective eigenstates are labelled by the total spin S and its projection M_S, which are defined from $\mathbf{S}^2|S,M_S\rangle = S(S+1)|S,M_S\rangle$ and $S_z|S,M_S\rangle = M_S|S,M_S\rangle$. Then, the decay rate is given by $\Gamma/\Gamma_0 = S(S+1)+M_S(1-M_S)$. One can check how the most superradiant state is given by $S=N/2$ and $S_z=0$, *i.e.*, a fully symmetric state with half of the atoms excited, for which the decay rate becomes $\Gamma=N(N+1)\Gamma_0/4$, leading to an emitted intensity $\sim N^2\Gamma_0$, for a large enough number of atoms. Instead, completely dark states with $\Gamma=0$ are given by $M_S=-S$, in particular the total singlet state $S=M_S=0$ is a dark state.

While this construction does not break completely the degeneracies, it organizes the eigenstates in the so-called many-body Dicke ladder, naturally revealing the appearance of collective radiative states (see Fig. 4). The N spin-1/2 physics are described by a (reducible) representation of the SU(2) group. Here, there are three group generators that correspond to the Pauli matrices, satisfying the following commutation relations: $\left[S^a, S^b\right] = i\epsilon^{abc}S^c$, with $\{a, b, c\} = \{x, y, z\}$ and ϵ^{abc} the totally antisymmetric Levi-Civita symbol. In this case, there is just a single independent Casimir operator (group invariant), which corresponds exactly to the total spin operator S^2. Its eigenvalues S uniquely label the irreducible representations of the group, each of dimension $2S+1$. In the Dicke problem, irreducible representations (different S sectors) are not mixed by dynamics of Eq. (7) (see Section 5).

In general, we can always numerically evaluate the Hamiltonian $\mathcal{H}_{\text{eff}}$ using exact diagonalization. Due to degeneracy in each sector (S, M_S), the obtained states are not necessarily of the Dicke form. It is important that we force the computational program to build permutationally invariant states, otherwise they we will not get the right results.

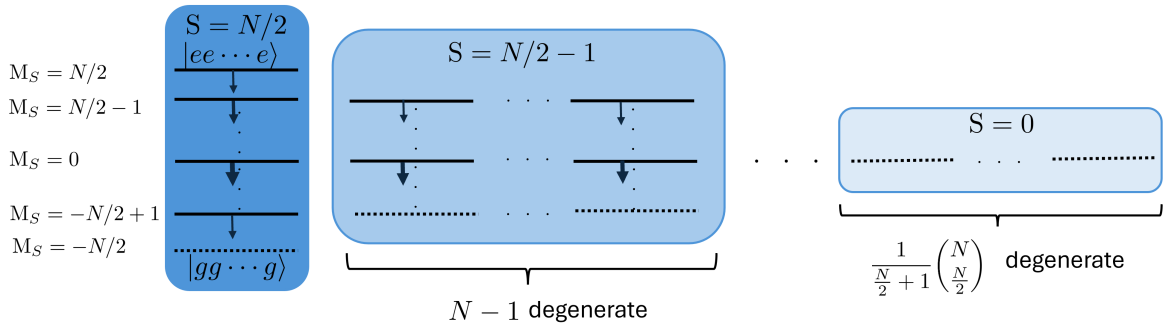

Figure 4: **Dicke many-body ladder for N 2-level atoms**, with N even. Different colours represent different irreducible representations of SU(2) spanned by different values of S. In every irreducible representation, there are different levels from $M_S \in [-S, S]$. Arrows represent the natural decay of these levels following Eq. (7), and thick arrows describe states with bigger decay rate. Levels represented by dotted lines are completely dark states.

4.1.2 Λ atoms: SU(3) mapping

We now generalize the discussion to Λ-type atoms, and find the quantum numbers that describe the collective eigenmodes and decay rates in this more complex case as the main novelty of our work. Now, the SU(2) representation is insufficient because of the richer three-level structure. A complete description requires the full SU(3) algebra including the spin operators and the so-called quadrupole operators [61, 62, 63]. For convenience, and without loss of generality, we will label the basis states as:

$$|g_1\rangle = \begin{pmatrix}1\\0\\0\end{pmatrix}, \quad |g_2\rangle = \begin{pmatrix}0\\1\\0\end{pmatrix}, \quad |e\rangle = \begin{pmatrix}0\\0\\1\end{pmatrix}.$$

While in SU(2), the only group invariant is the total spin operator S^2, in SU(3) there are two independent Casimir operators. The quadratic Casimir operator is defined as:

$$\mathbf{C}^2 = \sum_{i=1}^{8} \lambda_i \cdot \lambda_i, \tag{18}$$

where $\{\lambda_i\}$ are the group generators. Note that the choice of generators $\{\lambda_i\}$ is not unique: any complete basis of the SU(3) algebra related by a unitary transformation can be used. The quadratic Casimir operator is basis-independent, however, its explicit form and eigenvalues depend on the normalization

convention for the generators. Instead of spin-1 and quadrupole operators, we will choose here the Gell-Mann matrices as the eight group generators (see Appendix B.1). The cubic Casimir operator is used to distinguish between an irreducible representation and its conjugate, but it will not be used for our purposes.

Any irreducible representation of SU(3) can be labeled by their Dynkin coordinates (p,q) (see Appendix. B.2). In any irreducible representation, the quadratic Casimir operator (Eq. 18) is proportional to the identity, $\mathbf{C}^2 = C_2(p,q)\mathbf{1}$, with eigenvalue:

$$C_2(\mathrm{p},\mathrm{q}) = \frac{1}{3}\left(p^2+q^2+pq+3p+3q\right), \tag{19}$$

and the dimension of each representation is given by $\frac{1}{2}(p+1)(q+1)(p+q+2)$. The fundamental representation of one three-level system is represented by: $(\mathrm{p},\mathrm{q}) = (1,0)$. Coupling many Λ-atoms, requires Young tableaux instead of Clebsch-Gordan coefficients to get the possible values of (p,q) (see Appendix. B.2)

Now we will work with the Dicke dissipative Hamiltonian given by Eq. (16a) and express it in terms of SU(3) generators. The different single-atom raising and lowering operators can be written in terms of the Gell-Mann matrices as: $\hat{\sigma}^{eg_1} = \frac{1}{2}(\lambda_4 - i\lambda_5)$, $\hat{\sigma}^{g_1e} = \frac{1}{2}(\lambda_4 + i\lambda_5)$, $\hat{\sigma}^{eg_2} = \frac{1}{2}(\lambda_6 - i\lambda_7)$ and $\hat{\sigma}^{g_2e} = \frac{1}{2}(\lambda_6 + i\lambda_7)$. As done for the spin operators in the two-level case, we can define the collective Gell-Mann matrices as: $\Lambda_a = \sum_{i=1}^{N}\lambda_a^i$, where the super-index i denotes the Gell-Mann matrix acting on site i. Using the commutation relations $[\Lambda_4,\Lambda_5] = i(\Lambda_3+\sqrt{3}\Lambda_8)$, $[\Lambda_6,\Lambda_7] = i(-\Lambda_3+\sqrt{3}\Lambda_8)$ and the definition of the quadratic Casimir operator (Eq. 18) the effective Hamiltonian becomes:

$$\mathcal{H}_{\text{eff}} = -i\frac{\Gamma_0}{2}\frac{1}{4}\left(\mathbf{C}^2 - \Lambda_1^2 - \Lambda_2^2 - \Lambda_3^2 - \Lambda_8^2 - 2\sqrt{3}\Lambda_8\right). \tag{20}$$

The degeneracy of the ground states implies a symmetry under $|g_1\rangle \leftrightarrow |g_2\rangle$, which can be exploited by introducing an equivalent SU(2) subalgebra within $\{g_1,g_2\}$ subspace. In this case, $\mathrm{S}^x_{g_1,g_2} = \frac{1}{2}\Lambda_1$, $\mathrm{S}^y_{g_1,g_2} = \frac{1}{2}\Lambda_2$ and $\mathrm{S}^z_{g_1,g_2} = \frac{1}{2}\Lambda_3$, so that: $4\mathrm{S}^2_{g_1,g_2} = \Lambda_1^2+\Lambda_2^2+\Lambda_3^2$. Using the definition of Λ_8 in terms of the occupation number operators: $\Lambda_8 = 1/\sqrt{3}\left(\hat{\mathrm{N}}_{g_1}+\hat{\mathrm{N}}_{g_2}-2\hat{\mathrm{N}}_e\right)$ and the relationship between the population in the different levels: $\hat{\mathrm{N}} = \hat{\mathrm{N}}_{g_1}+\hat{\mathrm{N}}_{g_2}+\hat{\mathrm{N}}_e$, we obtain a compact form for the effective Hamiltonian:

$$\mathcal{H}_{\text{eff}} = -i\frac{\Gamma_0}{2}\left[\mathbf{C}^2 - \mathrm{S}^2_{g_1,g_2} - \frac{1}{12}\left(\hat{\mathrm{N}}-3\hat{\mathrm{N}}_e\right)^2 - \frac{1}{2}\left(\hat{\mathrm{N}}-3\hat{\mathrm{N}}_e\right)\right]. \tag{21}$$

This expression shows that the collective eigenmodes and decay rates are characterized by the following quantum numbers: the quadratic Casimir eigenvalue $C_2(p,q)$, the total spin associated with the $\{g_1,g_2\}$ SU(2) subalgebra, the total number of particles N, and the total number of excited sites $N_e \equiv \langle\sigma_{ee}\rangle \equiv \langle\sum_i \hat{\sigma}_i^{ee}\rangle$. Moreover, the population imbalance between the two ground states $N_{g_1} - N_{g_2} \equiv 2\langle S_z^{g_1g_2}\rangle$ also commutes with $\mathcal{H}_{\text{eff}}$, and thus, the eigenstates can always be chosen with well defined values of N_e, N_{g_1} and N_{g_2}.

As a consistency check, we first analyse the simplest case of a single Λ-atom ($N=1$), corresponding to the fundamental representation $(\mathrm{p},\mathrm{q}) = (1,0)$ with $C_2 = 4/3$. In this case: $\mathcal{H}_{\text{eff}}|g_1\rangle = 0$, $\mathcal{H}_{\text{eff}}|g_2\rangle = 0$ and $\mathcal{H}_{\text{eff}}|e\rangle = -i\Gamma_0|e\rangle$. Therefore $|e\rangle$ has a decay rate of $2\Gamma_0$, as expected for a single atoms with two independent decay channels, each with rate Γ_0.

Moreover, using the Hamiltonian Eq. (21) we can check the prediction in [47]. In this work, authors show that for $N-1$ optical transitions, at least N atoms are needed for the emergence of a single-excitation dark state, which necessarily has the form:

$$|\psi^N_{\text{dark}}\rangle = \frac{1}{\sqrt{N!}}\sum_{\pi\in S_N}\text{sgn}(\pi)\pi\left(|g_1...g_{N-1}e\rangle\right), \tag{22}$$

where the sum runs over all permutations π of N elements. This is a completely antisymmetric state for a given configuration. For our Λ-type atoms, this means that we need at least $N = 3$ atoms to find this completely antisymmetric state: $|\psi^3_{\text{dark}}\rangle = \frac{1}{\sqrt{6}}(-|eg_1g_2\rangle + |eg_2g_1\rangle + |g_1eg_2\rangle - |g_2eg_1\rangle - |g_1g_2e\rangle + |g_2g_1e\rangle)$. We found that this state corresponds exactly to the irreducible representation (p,q) $= (0, 0)$.

Dicke-decaying diagrams are the extension from Dicke-many body ladder of two-level atoms to Λ-atoms, where the states are now labelled by the excitation number $\langle\sigma_{ee}\rangle$ and the ground state imbalance $\langle \mathrm{S}_z^{g_1g_2}\rangle$. Here the states are represented by dots instead of lines (in contrast to the two-level atom case). The fundamental Dicke-decaying diagram for $N = 1$ is shown in Fig. 5, where the states are just $|g_1\rangle$, $|g_2\rangle$ and $|e\rangle$.

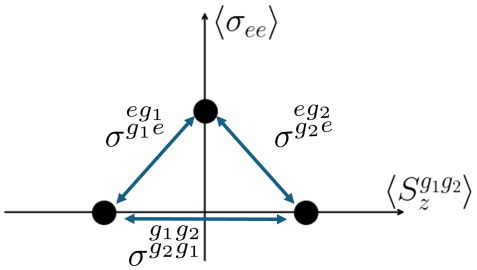

Figure 5: Fundamental diagram with the eigenvalues of $\sigma_{ee} \equiv \hat{\mathbf{N}}_e$ and $\mathrm{S}_z^{g_1g_2} \equiv \hat{\mathbf{N}}_{g_1} - \hat{\mathbf{N}}_{g_2}$ labelling the three possible states. The action of the ladder operators is also shown.

In Fig. 6 we show the Dicke-decaying diagram in the more complicated case of $N = 3$ atoms. The corresponding transition rates following Eq. 13. One can see the different irreducible representations and the appearance of the predicted single excitation dark state in the $(p, q) = (0, 0)$ representation.

As the atom number increases beyond $N = 3$, more dark states start to appear in the single excitation sector. However, to observe a dark state in the two-excitations sector, one requires at least $N = 6$. Likewise, a dark state with three excitations appears at $N = 9$, and so on. This follows from he fact that subradiant states in higher-excitation sectors arise only in the $(\mathrm{p}, \mathrm{q}) = (0, 0)$ irreducible representation, which emerges in multiples of 3.

As another example, we now consider $N = 6$ atoms, with the following irreducible representations: $5(0, 0) \oplus 16(1, 1) \oplus 5(0, 3) \oplus 10(3, 0) \oplus 9(2, 2) \oplus 5(4, 1) \oplus (6, 0)$, where the prefactor in (p, q) indicates the multiplicity of the representation. The symmetric subspace (6,0) contains the fully symmetric Dicke-decaying diagram, while the five copies of (0,0) show the appearance of dark-states in the two-excitations manifolds. The corresponding Dicke decaying diagrams are shown in Appendix. B.3.

We note that this model can be easily generalized to any atomic structure with one excited state and n degenerate ground states. In this case the SU$(n + 1)$ group representation is needed, but the quadratic Casimir operator involving the square of the group generators will be enough to describe the effective Hamiltonian of the system.

4.1.3 Entanglement in collective eigenmodes

To characterize the entanglement content of collective Dicke states, we use two bipartite measures: the Von-Neumann entropy and the negativity. In this case, the total atomic system is divided into two different subsystems A and B, with Hilbert space dimensions $\dim(\mathcal{H}_A) = d_A$ and $\dim(\mathcal{H}_B) = d_B$.

The Von-Neumann entropy (or entropy of entanglement) is well defined for pure states, $\rho_{AB} = |\Psi\rangle^{AB}\langle\Psi|^{AB}$, and reads:

$$E_S(\rho) = S(\rho_A) = -\mathrm{Tr}\left(\rho_A \log \rho_A\right), \tag{23}$$

where $\rho_A = \mathrm{Tr}_B(\rho_{AB})$ is the reduced density matrix for subsystem A. Notice that $S(\rho_A) = S(\rho_B) = -\mathrm{Tr}\left(\rho_B \log \rho_B\right)$. If $E_S(\rho) = 0$ the state is separable, otherwise, for $E_S(\rho) > 0$, the state is entangled.

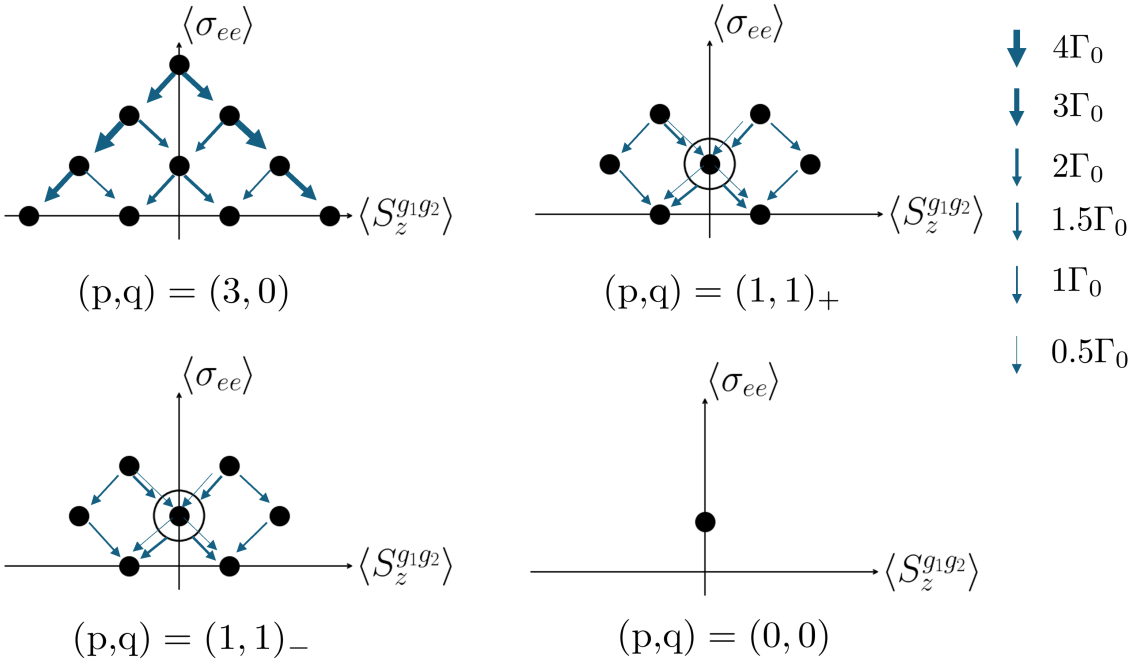

Figure 6: **Dicke-decaying diagrams for N = 3 Λ-type atoms.** One can see four disconnected ladders coming from the different irreducible representations. Top left panel with $(p, q) = (3, 0)$ represents the symmetric subspace where the dynamics are restricted given an initial state with all atoms inverted, i.e., $|e\rangle^{\otimes N}$ (represented by the top point), see also Section 5.1. The irreducible representations with $(p, q) = (1, 1)$ show mixed symmetries between the different Young tableaux, showing two degenerate states represented by the circle around the dot. Bottom right panel with $(p, q) = (0, 0)$ represents the completely antisymmetric sector with just one dark single-excitation state, as predicted in Eq. 22. Arrows represent the possible decays from one state into the others, with a width that is proportional to the rate evaluated from Eq. (13), as indicated in the legend.

Maximally entangled states have an entropy of entanglement $E_S = \log_2(d)$, where $d = \min(d_A, d_B)$.

Negativity [64] is particularly useful for mixed states (see Section 5). It is related to the Peres-Horodecki criterion (positive under partial transpose, PPT) for separability [65]. This criterion states that if ρ is separable, then its partial transpose with respect to subsystem A, ρ^{T_A}, has only non-negative values. It is an entanglement witness, meaning that it is a sufficient, but not necessary condition for bipartite entanglement, except for 2×2 and 2×3 systems, where it becomes both necessary and sufficient [66, 67]. The negativity is defined as:

$$\mathcal{N}(\rho) = \sum_i \frac{|\lambda_i| - \lambda_i}{2}, \tag{24}$$

where λ_i are all the eigenvalues of ρ^{T_A}. Therefore, the negativity is the absolute sum of the negative eigenvalues in ρ^{T_A}. An alternative and derived measure is the logarithmic negativity, given by:

$$E_N(\rho) = \log(2\mathcal{N} + 1). \tag{25}$$

For pure states, it can be shown that $E_N(\rho) \geq E_S(\rho)$, with equality holding for maximally entangled states and product states (see Appendix. C).

In Fig. 7(a) we show the entanglement entropy and logarithmic negativity as a function of the number of excitations for $N = 6$ two-level atoms under the bipartition $1|(N-1)$, *i.e.* quantifying how a single atom is entangled with the remaining N - 1 for every Dicke state. We can see how all the states with the same number of excitations have the same bipartite entanglement. This bipartition is also chosen because it allows for an analytical expression for the reduced density matrix: $\rho_A = \frac{N_e}{N}|e\rangle\langle e| + \frac{N-N_e}{N}|g\rangle\langle g|$, and

therefore the entanglement entropy can be evaluated explicitly as:

$$E_S(\rho) = -\frac{N_e}{N}\log_2\left(\frac{N_e}{N}\right) - \left(1-\frac{N_e}{N}\right)\log_2\left(1-\frac{N_e}{N}\right). \tag{26}$$

Thus, the entanglement is directly connected to the Hilbert space dimension of the Hamiltonian blocks with a fixed number of excitations, showing a bigger entanglement for $N_e = N/2$. We note that among these states, there are the most superradiant and dark collective modes, as previously discussed. Moreover, one observes that the inequality $E_N(\rho) \geq E_S(\rho)$ is satisfied.

In Fig. 7(b) we show the entanglement entropy for $N = 6$ Λ-type atoms and a bipartition $1|(N-1)$, now as a function of both the number of excitations and the population imbalance between the two ground states. We can see how all the states with the same number of excitations and population imbalance have the same bipartite entanglement. We do not show the logarithmic negativity, as it exhibits the same qualitative behaviour. The reduced density matrix takes now the form: $\rho_A = \frac{N_e}{N}|e\rangle\langle e| + \frac{N_{g_1}}{N}|g_1\rangle\langle g_1| + \frac{N_{g_2}}{N}|g_2\rangle\langle g_2|$, leading to the entanglement entropy expression:

$$\begin{aligned} E_S(\rho) = -\frac{N_e}{N}\log_2\left(\frac{N_e}{N}\right) - \left(\frac{N-N_e+\langle \mathrm{S}_z^{g_1g_2}\rangle}{2N}\right)\log_2\left(\frac{N-N_e+\langle \mathrm{S}_z^{g_1g_2}\rangle}{2N}\right) \\ - \left(\frac{N-N_e-\langle \mathrm{S}_z^{g_1g_2}\rangle}{2N}\right)\log_2\left(\frac{N-N_e-\langle \mathrm{S}_z^{g_1g_2}\rangle}{2N}\right). \end{aligned} \tag{27}$$

As before, maximal entanglement corresponds to the largest Hilbert space dimension. In the case of $N = 6$, it corresponds to $N_e = 2$ and $\langle S_z^{g_1g_2}\rangle = 0$, precisely where the most superrradiant states and subradiant states in the two-excitation manifold are located.

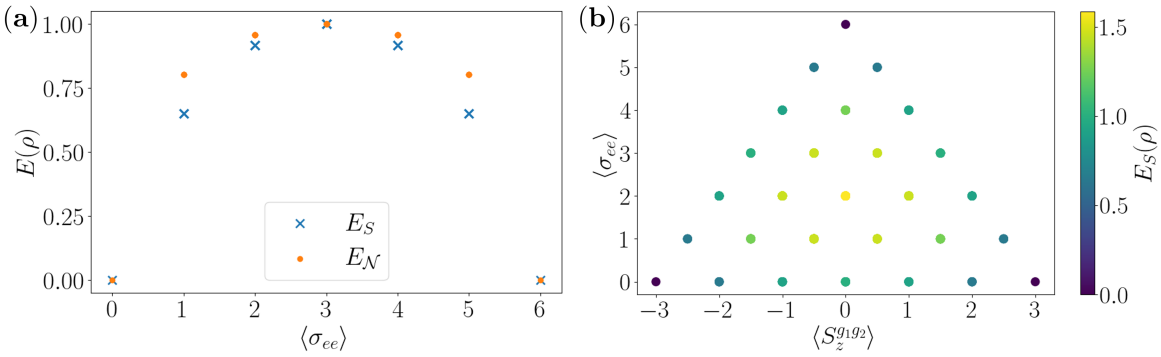

Figure 7: **Entanglement properties of Dicke states.** **(a)** Entanglement entropy and logarithmic negativity as a function of the number of excitations (note that $\langle\sigma_{ee}\rangle = N_e$) for N = 6 two-level atoms. **(b)** Entanglement entropy as a function of the number of excitations $\langle\sigma_{ee}\rangle$ and the ground state population imbalance $\langle \mathrm{S}_z^{g_1g_2}\rangle$ for N = 6 Λ-type atoms.

4.2 Finite-size model in presence of coherent interactions

We now move to the case where the atoms are separated by finite distances, beyond the point-like gas or Dicke limit previously discussed. For finite size systems, permutational invariance no longer holds. Now, the dissipative and dispersive couplings given by Eq. (10a) and Eq. (10b) have different values depending on the pair of atoms i, j and the atomic transitions q, q'. In the case of the considered geometries, the ring eigenstates are also permutationally invariant due to symmetry $[\mathbf{J}, \mathbf{\Gamma}] = 0$, showing a smooth crossover between the Dicke model and finite-size effects. For the chain, and more general geometries, coherent and dissipative interactions do not commute $[\mathbf{J}, \mathbf{\Gamma}] \neq 0$, and therefore the collective eigenstates are not simply the dissipative Dicke states described before. Nevertheless, the collective behaviour can be understood by diagonalizing the effective Hamiltonian in Eq. (11), using the previous Dicke basis as a reference.

In Fig. 8 (a) we show the minimum and maximum decay rates in the single-excitation manifold as a function of the inter-particle distance d for both geometries considered (ring and chain), comparing two-level and Λ-type atoms for $N = 3$ atoms. One can observe collective radiance effects. In all cases, for $d/\lambda_0 \gg 1$, atoms behave independently and the single-channel decay rate Γ_0 is recovered. In the Dicke limit $d/\lambda_0 \ll 1$, one recovers the decay rates predicted in the previous section and spontaneous emission in each channel can get enhanced or suppressed. Between these two regimes, a smooth crossover with oscillations can be observed. Subradiant behaviour is recovered in all geometries and atomic structures. In contrast, superradiance effects in each channel are weaker for Λ-type atoms in the single-excitation manifold. However, when adding the two channels one gets a bigger decay than for the two-level case.

In Fig. 8 (b) we study finite-size effects by showing the minimum decay rate in the single-excitation sector as a function of the atom number N, for a fixed $d/\lambda_0 = 0.08$ and both geometries. As expected, the closed geometry (ring) is less sensitive to finite-size effects than open chains, because for the closed geometry the radiation does not escape through the ends of the chains. The presence of multiple decay channels in Λ-atoms increases the minimum decay rate compared to the two-level case.

Finally, in Fig. 8 (c) we test the prediction from Section 4.1.2. Here, we show that at least $N = 6$ atoms are required to obtain subradiant states with two excitations in Λ-atoms. For the two-level case one needs at least $N = 4$ atoms. The plot shows the minimum decay rate in the two-excitation manifold for a ring of two-level and Λ-atoms at the same fixed interparticle distance $d/\lambda_0 = 0.08$. For $N \geq 6$, dark states with $\Gamma \to 0$ start to appear in Λ-atoms, while in the two-level case is for $N \geq 4$ as expected. The inset highlights the logarithmic scaling of the minimum decay rate for $N \geq 6$, showing that larger systems further suppress decay, as happened in Fig. 8 (b) for the single excitation sector.

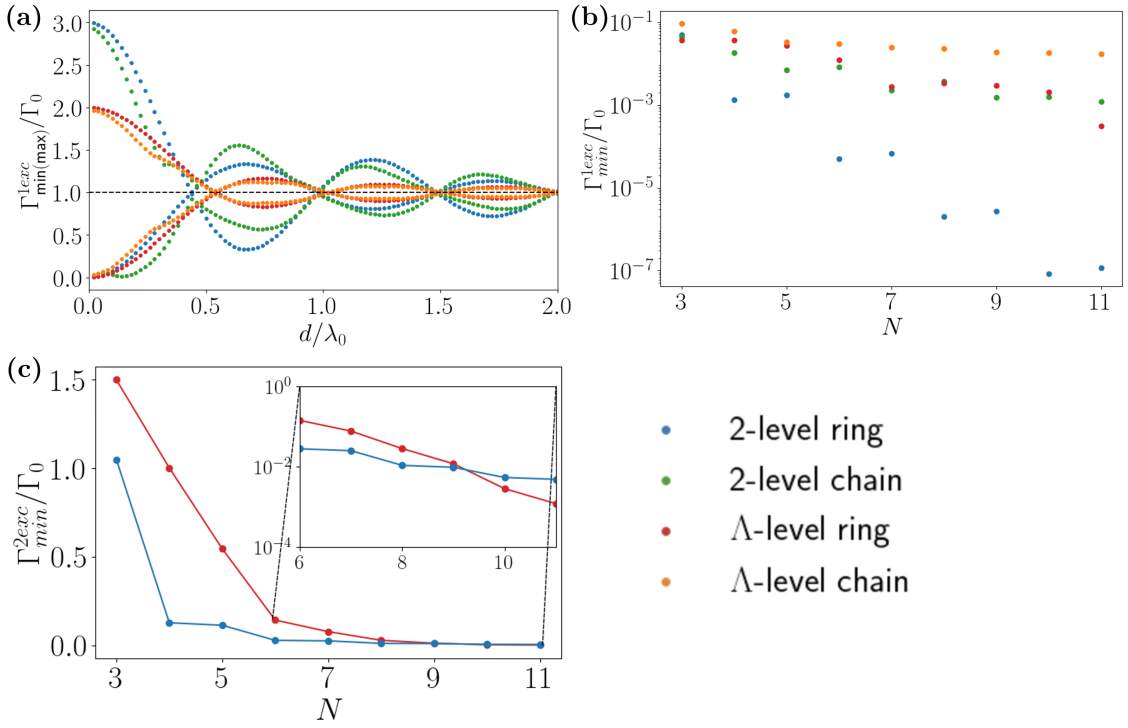

Figure 8: **Collective decay rates in the finite size model in presence of coherent interactions. (a)** Minimum and maximum decay rate in the single-excitation manifold as a function of the interparticle distance d/λ_0, comparing the ring and chain geometries for the two-level and Λ-type atoms with $N = 3$. **(b)** Minimum decay rate in the single-excitation manifold as a function of the atoms number N, for $d/\lambda_0 = 0.08$ in both geometries and atomic structure. **(c)** Minimum decay rate in the two-excitation manifold as a function of N for Λ-atoms in a ring at $d/\lambda_0 = 0.08$. The inset, in logarithmic scale, shows the emergence of subradiant states for $N \geq 6$.

5 Dynamics

In this Section we analyse the dynamics of the open quantum spin model for Λ-atoms and starting from an initially fully inverted population. We first consider the dissipative Dicke model (Section 5.1) to understand the main features of dynamics. We then include finite-size and coherent effects (Section 5.2) with a particular focus on the time evolution of the entanglement content between the atoms. Finally, we study how the steady-state entanglement changes with respect to the model parameters and analyse some of its properties (Section 5.2.2).

5.1 Dissipative Dicke model

We begin by analysing the dynamics in the dissipative Dicke model (see Section 3.4). As shown in Appendix D, the evolution generated by Eq. (7) does not mix different SU(3) irreducible representations when the system is initialized with well-defined Dynkin labels (p,q). Interestingly, this result can be easily generalized for any atomic structure with n degenerate ground states and their respective SU$(n+1)$ irreducible representations.

As a representative example, see Fig. 9. Here, we show the dynamics of $N = 3$ Λ-type atoms starting with the fully inverted state $|eee\rangle$. This state belongs to the symmetric irreducible representation $(3, 0)$ (see Fig. 6 top left panel). As a consequence, the dynamics is confined to this symmetric sector, and populations decay only in it.

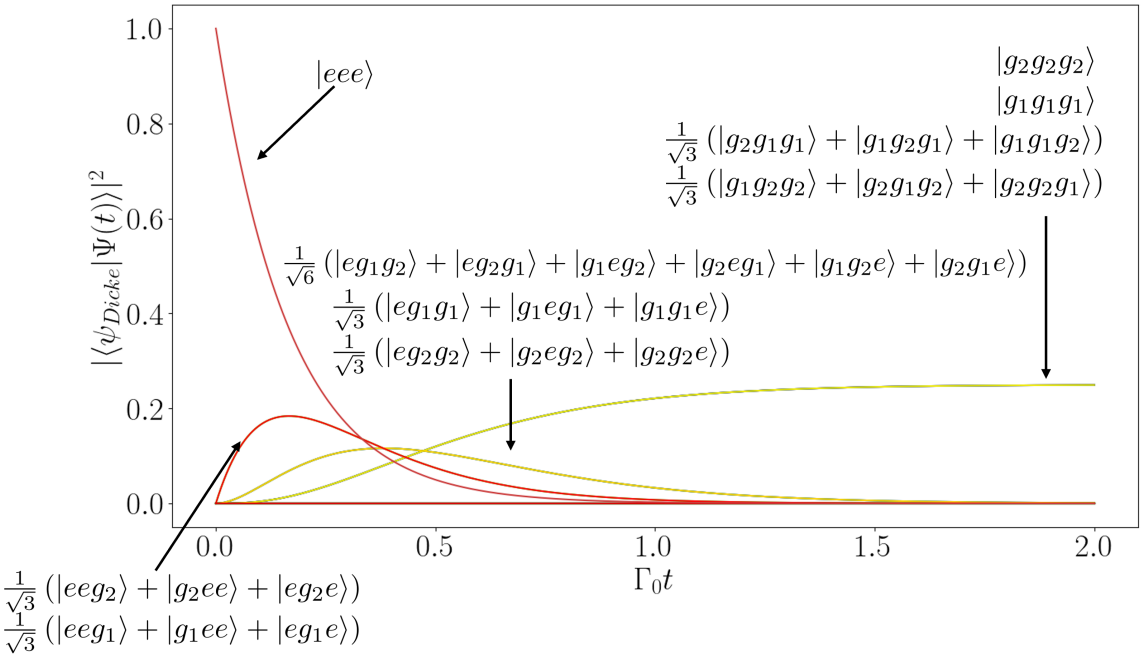

Figure 9: **Dynamics in the Dicke model.** Time evolution of $N = 3$ Λ-type atoms in the dissipative Dicke model, starting from fully inverted population: $\rho(t = 0) = |eee\rangle\langle eee|$. Since this state belongs to the symmetric irreducible representation with (p,q) $= (3, 0)$, the dynamics remain confined to this sector and only symmetric states are populated. Superposed lines indicate equal population between the corresponding states.

5.2 Finite-size model in presence of coherent interactions

Departing from the Dicke limit, where all particles are effectively at the same point, introduces finite-size effects due to non-zero inter-particle separations. In this regime, both the distance-dependent dissipative couplings and the coherent interactions (which no longer commute with the dissipative part) break the conservation of irreducible representations that characterizes the Dicke-model dynamics. Consequently, even if we start with a fully inverted initial state $|\Psi(t=0)\rangle = |e\rangle^{\otimes N}$, dynamics can populate states outside the perfectly smmetric Dicke ladder. To analyze these effects, we consider $N = 6$ atoms trapped in the ring geometry for both the two-level and Λ-level configurations. This choice minimizes boundary effects, as discussed in Section 4.2.

5.2.1 Dicke superradiance and entanglement dynamics

One key concept with the dynamics happening completely or almost in the symmetric sector is Dicke superradiance. During the decay along these states with the maximum decay rate, the system undergoes a superradiant burst: a peak in the photon emission rate $R(t)$ proportional to N^2 [17, 19], coming from the constructive interference of the atomic dipoles. This peak marks the moment when atoms are most strongly correlated. An interesting question is the relation between this photon-emission burst and the interatomic entanglement generation within the process, which we analyse in the following.

In Fig. 10 (a) we plot the logarithmic negativity (Eq. 25) as a function of time for different interparticle distances, together with the Dicke limit result, for comparison. For all cases we observe an initial peak of entanglement at short times, which is higher in the Dicke limit.

In Fig. 10 (b) we also plot the photon-emission rate from Eq. (14). At small enough inter-particle separation, even for small N, one observes the superradiant burst peak in the emission rate. At larger separations ($d/\lambda_0 = 0.5$) the burst disappears and the emission follows the independent-atom exponential decaying law. For Λ atoms, the burst is more pronounced than in the two-level case, reflecting stronger cooperative effects.

Interestingly, we find that the peak in entanglement precisely coincides with the superradiant burst in the photon emission rate. The simultaneous maximization of emission and entanglement generation seems natural, as cooperative photon emission enhances correlations among the atoms, leading to enhanced entanglement.

As the interparticle distance increases, atoms start to behave more independently, leading to a burst and maximum entanglement suppression. Interestingly, Λ-type atoms sustain a finite steady-state entanglement, in contrast to two-level atoms. The reason is that while two-level atoms decay into the trivial pure ground state $|g\rangle^{\otimes N}$, Λ atoms decay into a mixture within the ground-state manifold, where some collective states are entangled (see Fig. 7). Before reaching the steady-state entanglement, as d/λ_0 increases there is a valley where entanglement negativity vanishes.

For completeness, we also plot in Fig. 10 (c) the purity $\mathcal{P} = \mathrm{Tr}(\rho^2)$ of the density matrix as a function of time for different distances and the Dicke model. Starting from a pure state ($\mathcal{P} = 1$), the purity decreases as the density matrix becomes a mixed state ($\mathcal{P} < 1$) and reaches a minimum value at the superradiant peak, when the state is maximally mixed. For the two-level atoms in the Dicke limit, the purity quickly returns to the unity once all atoms decay to the ground state. At finite distances, coherent interactions and finite-size effects populate other states leading to a slower recovery. For Λ atoms, the steady state remains mixed in all cases, consistent with the presence of an steady-state entanglement due to the population of many ground state manifold states.

5.2.2 Steady-state entanglement and purity

Once the full dynamics is studied, we analyse the steady state entanglement and purity depending on the interparticle distance. The steady state can be obtained by directly diagonalizing the Liouvillian superoperator [68], rather than evolving the system in time until the density matrix derivatives vanish, which is generally more computationally demanding.

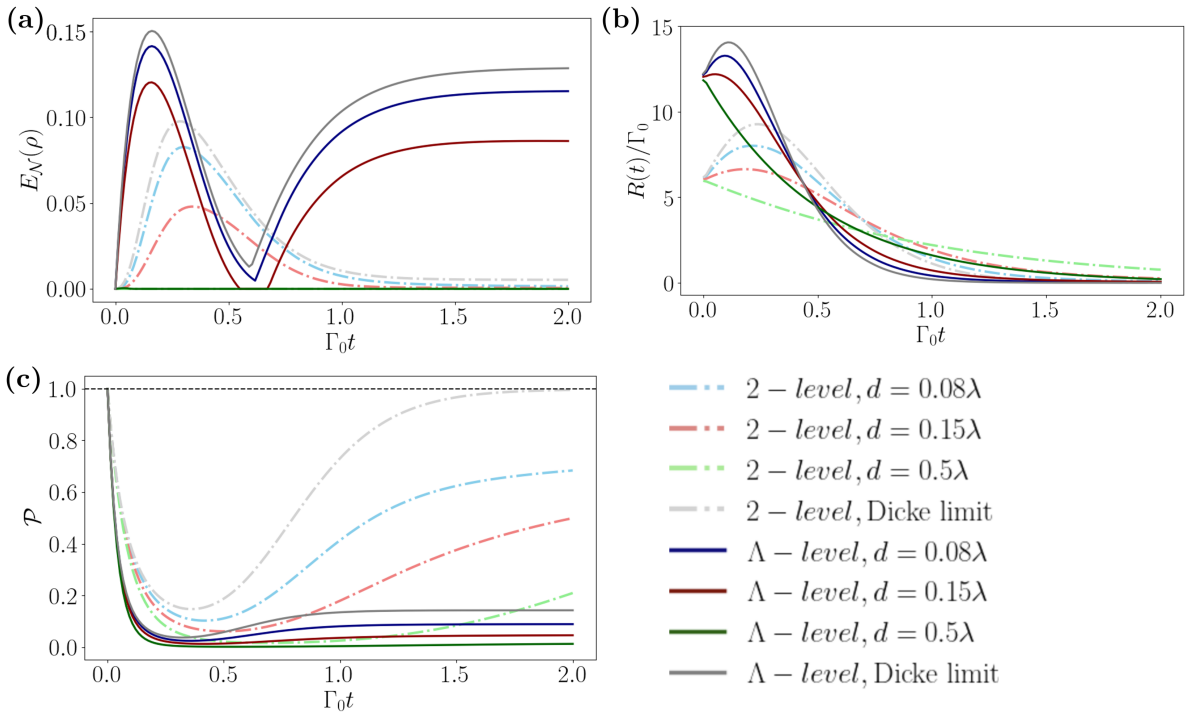

Figure 10: **Dynamics entanglement with finite-size and coherent effects. (a)** Logarithmic negativity as a function of time for different interparticle distances and for the Dicke model. **(b)** Photon emission rate as a function of time. **(c)** Purity of the density matrix, $\mathcal{P} = \mathrm{Tr}(\rho^2)$, as a function of time. The figures illustrate how finite-size and coherent interaction effects modify the ideal Dicke superradiant dynamics. All plots are done for $N = 6$ atoms trapped in a ring geometry.

For this algorithm, it is convenient to flatten the density matrix as a column vector. For instance, in the case of a qubit one has:

$$\rho = \begin{pmatrix} \rho_{11} & \rho_{12} \\ \rho_{21} & \rho_{22} \end{pmatrix} \rightarrow |\rho\rangle = \begin{pmatrix} \rho_{11} \\ \rho_{12} \\ \rho_{21} \\ \rho_{22} \end{pmatrix}, \tag{28}$$

where now $|\rho\rangle$ is a vector written in the Dirac notation. The initial state will be: $|\rho(0)\rangle = \text{flatten}(|\Psi_0\rangle\langle\Psi_0|)$.

The Liouvillian superoperator $\mathcal{O} = \mathcal{K} + \mathcal{J}$, which generates the dynamics, can be constructed through the tensor product operation between the flattened density matrix and the corresponding atomic raising and lowering operators, combined with identity operators to ensure dimensional consistency. For example, when multiplying a density matrix by a general matrix A from either side, the mapping becomes:

$$A\rho \rightarrow \hat{A}|\rho\rangle = (\mathbf{1} \otimes A)|\rho\rangle, \qquad \rho A \rightarrow |\rho\rangle\hat{A} = (A^T \otimes \mathbf{1})|\rho\rangle, \tag{29}$$

where $\mathbf{1}$ has the same dimensions as A. Consequently, the Liouvillian superoperator has size $(3^N)^2 \times (3^N)^2$, which quickly becomes computationally demanding for large N. Now, the equation governing dynamics in this flattened form reads:

$$\frac{\partial|\rho\rangle}{\partial t} = \hat{\mathcal{O}}|\rho\rangle. \tag{30}$$

Diagonalizing $\hat{\mathcal{O}}$ yields its eigenvalues and right/left eigenvectors. Since $\hat{\mathcal{O}}$ is non-Hermitian, eigenvectors are biorthogonal: $\hat{\mathcal{O}}|v_i^R\rangle = \lambda_i|v_i^R\rangle$ and $(|v_i^L\rangle)^\dagger\hat{\mathcal{O}} = \lambda_i(|v_i^L\rangle)^\dagger$. Hence the decomposition is:

$$\hat{\mathcal{O}} = \sum_{i}^{(3^N)^2} \lambda_i |v_i^R\rangle\langle v_i^L|. \tag{31}$$

At any time, the density matrix can be found using this formalism as:

$$|\rho(t)\rangle = e^{\hat{\mathcal{O}}t}|\rho(0)\rangle = \sum_{i}^{(3^N)^2} e^{\lambda_i t}\langle v_i^L|\rho(0)\rangle|v_i^R\,\rangle. \tag{32}$$

To obtain the steady state we impose $\hat{\mathcal{O}}|\rho_{ss}\rangle = 0$. Thus, the steady state is reconstructed from the zero-eigenvalue subspace:

$$|\rho_{ss}\rangle = \sum_{i=1}^{r}\langle v_i^L|\rho(0)\rangle|v_i^R\rangle, \tag{33}$$

where the important point is that now the sum runs over all r eigenvectors with zero eigenvalue.

In Fig. 11 we analyse the steady-state logarithmic negativity and purity as functions of the interparticle distance d for $N = 6$ Λ atoms in a ring geometry. Panel (a) shows that for $d/\lambda_0 \gtrsim 0.4$ the logarithmic negativity vanishes, while in the Dicke limit it saturates to $E_{\mathcal{N}}(\rho_{ss}) \approx 0.13$. Panel (b) includes as reference a lower bound for the purity corresponding to a maximally mixed state in the ground state manifold, $1/2^N$. At large distances the system approaches this bound, while in the Dicke limit the symmetric ground manifold of $N = 6$ contains 7 states, leading to $\mathcal{P} = 1/7 \approx 0.143$, consistent with the observed result.

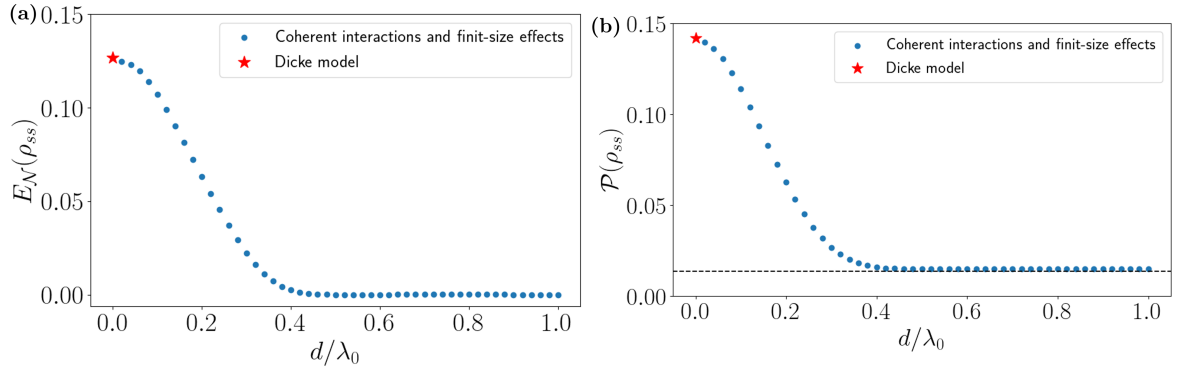

Figure 11: **Steady state properties as a function of interparticle distance. (a)** Steady-state logarithmic negativity as a function of the interpaticle distance. **(b)** Steady-state purity as a function of the interpaticle distance and the lower bound for a maximal mixed state of all ground state manifold. All plots are for $N = 6$ Λ atoms trapped in the ring configuration with the red star representing the Dicke model value.

6 Conclusions and Outlook

In this Master's Thesis, we investigated collective radiance properties of Λ-type atoms. To this end, we first developed a general formalism for multilevel atomic structures and then applied it to construct an open quantum spin model for Λ atoms with two coupled decay channels, where emission along one channel can induce excitations in the other.

We then analysed the Dicke model as a reference case. A central novelty of our approach was to map the problem onto $\mathrm{SU}(3)$ algebra, thereby extending the well-known Dicke ladder of two-level atoms to a generalized decay diagram for Λ atoms. This formalism predicts the emergence of n-excitation dark states when $N = 3n$, which we showed to be maximally entangled by evaluating both entanglement entropy and logarithmic negativity.

Next, we studied finite-size arrays in the presence of coherent interactions. We demonstrated that collective radiance persists, although the scaling with atom number is less favourable than in the two-level case. The ring geometry was found to be more robust against finite-size effects due to its higher symmetry. Interestingly, certain two-excitation states were identified as being darker in Λ atoms compared to their two-level counterparts.

When analysing the dynamics, we proved that in the Dicke model the evolution does not mix between different irreducible representations. For an initially inverted state, a superradiant burst appears in the photon emission rate, coinciding with the maximum of logarithmic negativity. An open question for future work is whether this connection is fundamental—i.e., whether the emission burst and peak entanglement always occur simultaneously—or whether their relation depends on system parameters, such as atom number and interparticle distance, or on the geometry or specific multilevel structure.

Another key observation is that entanglement disappears in the steady state for $d/\lambda_0 \gtrsim 0.4$, raising the question of whether this threshold marks the disappearance of the superradiant burst universally, or if it varies with geometry or atom number N.

Finally, this work suggests further avenues for engineering highly entangled dark states. Possible strategies include adding coherent driving fields or introducing detuning between atoms to break permutation symmetry, thereby enabling the preparation of purer entangled dark states.

Overall, the results presented here provide a comprehensive picture of collective phenomena in Λ-type atomic arrays. In particular, they may help interpret experimental observations in subwavelength arrays of atoms trapped by optical tweezers, where the excited state decays into two degenerate ground states through non-independent transitions.

Bibliography

[1] Steven Chu. Nobel lecture: The manipulation of neutral particles. *Reviews of Modern Physics*, 70(3):685–706, 1998.

[2] Claude N. Cohen-Tannoudji. Nobel lecture: Manipulating atoms with photons. *Reviews of Modern Physics*, 70(3):707–719, 1998.

[3] William D. Phillips. Nobel lecture: Laser cooling and trapping of neutral atoms. *Reviews of Modern Physics*, 70(3):721–741, 1998.

[4] Klemens Hammerer, Anders S. Sørensen, and Eugene S. Polzik. Quantum interface between light and atomic ensembles. *Reviews of Modern Physics*, 82(2):1041–1093, 2010.

[5] D. J. Wineland, J. J. Bollinger, W. M. Itano, F. L. Moore, and D. J. Heinzen. Spin squeezing and reduced quantum noise in spectroscopy. *Physical Review A*, 46(11):R6797–R6800, 1992.

[6] L.-M. Duan, M. D. Lukin, J. I. Cirac, and P. Zoller. Long-distance quantum communication with atomic ensembles and linear optics. *Nature*, 414(6862):413–418, 2001.

[7] Immanuel Bloch, Jean Dalibard, and Wilhelm Zwerger. Many-body physics with ultracold gases. *Reviews of Modern Physics*, 80(3):885–964, 2008.

[8] Manuel Endres, Hannes Bernien, Alexander Keesling, Harry Levine, Eric R. Anschuetz, Alexandre Krajenbrink, Crystal Senko, Vladan Vuletic, Markus Greiner, and Mikhail D. Lukin. Atom-by-atom assembly of defect-free one-dimensional cold atom arrays. *Science*, 354(6315):1024–1027, 2016.

[9] Daniel Barredo, Sylvain de Léséleuc, Vincent Lienhard, Thierry Lahaye, and Antoine Browaeys. An atom-by-atom assembler of defect-free arbitrary two-dimensional atomic arrays. *Science*, 354(6315):1021–1023, 2016.

[10] Daniel Barredo, Vincent Lienhard, Sylvain de Léséleuc, Thierry Lahaye, and Antoine Browaeys. Synthetic three-dimensional atomic structures assembled atom by atom. *Nature*, 561(7721):79–82, 2018.

[11] Immanuel Bloch. Ultracold quantum gases in optical lattices. *Nature Physics*, 1(1):23–30, 2005.

[12] M. Saffman. Quantum computing with atomic qubits and rydberg interactions: Progress and challenges. *Journal of Physics B: Atomic, Molecular and Optical Physics*, 49(20):202001, 2016.

[13] Hannes Bernien, Sylvain Schwartz, Alexander Keesling, Harry Levine, Ahmed Omran, Hannes Pichler, Soonwon Choi, Alexander S. Zibrov, Manuel Endres, Markus Greiner, Vladan Vuletić, and Mikhail D. Lukin. Probing many-body dynamics on a 51-atom quantum simulator. *Nature*, 551(7682):579–584, 2017.

[14] H. J. Kimble. The quantum internet. *Nature*, 453(7198):1023–1030, 2008.

[15] J. Perczel, J. Borregaard, D. E. Chang, H. Pichler, S. F. Yelin, P. Zoller, and M. D. Lukin. Topological quantum optics in two-dimensional atomic arrays. *Physical Review Letters*, 119(2):023603, 2017.

[16] Alexey V. Gorshkov, Axel André, Michael Fleischhauer, Anders S. Sørensen, and Mikhail D. Lukin. Universal approach to optimal photon storage in atomic media. *Physical Review Letters*, 98(12):123601, 2007.

[17] R. H. Dicke. Coherence in Spontaneous Radiation Processes. *Physical Review*, 93(1):99–110, 1954.

[18] R. H. Lehmberg. Radiation from an n-atom system. i. general formalism. *Physical Review A*, 2(3):883–888, 1970.

[19] M. Gross and S. Haroche. Superradiance: An essay on the theory of collective spontaneous emission. *Physics Reports*, 93(5):301–396, 1982.

[20] N. Skribanowitz, I. P. Herman, J. C. MacGillivray, and M. S. Feld. Observation of dicke superradiance in optically pumped hf gas. *Physical Review Letters*, 30(8):309–312, 1973.

[21] M. Gross, C. Fabre, P. Pillet, and S. Haroche. Observation of Near-Infrared Dicke Superradiance on Cascading Transitions in Atomic Sodium. *Physical Review Letters*, 36(17):1035–1038, 1976.

[22] H. M. Gibbs, Q. H. F. Vrehen, and H. M. J. Hikspoors. Single-pulse superfluorescence in cesium. *Physical Review Letters*, 39(9):547–550, 1977.

[23] R. G. DeVoe and R. G. Brewer. Observation of Superradiant and Subradiant Spontaneous Emission of Two Trapped Ions. *Physical Review Letters*, 76(12):2049–2052, 1996.

[24] J. A. Mlynek, A. A. Abdumalikov, C. Eichler, and A. Wallraff. Observation of dicke superradiance for two artificial atoms in a cavity with high decay rate. *Nature Communications*, 5(1):5186, 2014.

[25] P. Solano, P. Barberis-Blostein, F. K. Fatemi, L. A. Orozco, and S. L. Rolston. Super-radiance reveals infinite-range dipole interactions through a nanofiber. *Nature Communications*, 8(1):1857, 2017.

[26] Christian Liedl, Felix Tebbenjohanns, Constanze Bach, Sebastian Pucher, Arno Rauschenbeutel, and Philipp Schneeweiss. Observation of superradiant bursts in a cascaded quantum system. *Physical Review X*, 14(1):011020, 2024.

[27] Michelle O. Araújo, Ivor Krešić, Robin Kaiser, and William Guerin. Superradiance in a Large and Dilute Cloud of Cold Atoms in the Linear-Optics Regime. *Physical Review Letters*, 117(7):073002, 2016.

[28] G. Ferioli, A. Glicenstein, F. Robicheaux, R. T. Sutherland, A. Browaeys, and I. Ferrier-Barbut. Laser driven superradiant ensembles of two-level atoms near Dicke's regime. *Physical Review Letters*, 127(24):243602, 2021.

[29] Giovanni Ferioli, Antoine Glicenstein, Igor Ferrier-Barbut, and Antoine Browaeys. A non-equilibrium superradiant phase transition in free space. *Nature Physics*, 19(9):1345–1349, 2023.

[30] Giovanni Ferioli, Igor Ferrier-Barbut, and Antoine Browaeys. Emergence of Second-Order Coherence in the Superradiant Emission from a Free-Space Atomic Ensemble. *Physical Review Letters*, 134(15):153602, 2025.

[31] William Guerin, Michelle O. Araújo, and Robin Kaiser. Subradiance in a large cloud of cold atoms. *Physical Review Letters*, 116(8):083601, 2016.

[32] Giovanni Ferioli, Antoine Glicenstein, Loic Henriet, Igor Ferrier-Barbut, and Antoine Browaeys. Storage and release of subradiant excitations in a dense atomic cloud. *Physical Review X*, 11(2):021031, 2021.

[33] Stuart J. Masson, Igor Ferrier-Barbut, Luis A. Orozco, Antoine Browaeys, and Ana Asenjo-Garcia. Many-body Signatures of Collective Decay in Atomic Chains. *Physical Review Letters*, 125(26):263601, 2020.

[34] Stuart J. Masson and Ana Asenjo-Garcia. Universality of Dicke superradiance in arrays of quantum emitters. *Nature Communications*, 13(1):2285, 2022.

[35] Waseem S. Bakr, Jonathon I. Gillen, Amy Peng, Simon Fölling, and Markus Greiner. A quantum gas microscope for detecting single atoms in a Hubbard-regime optical lattice. *Nature*, 462(7269):74–77, 2009.

[36] Christian Gross and Waseem S. Bakr. Quantum gas microscopy for single atom and spin detection. *Nature Physics*, 17(12):1316–1323, 2021.

[37] Sandra Buob, Jonatan Höschele, Vasiliy Makhalov, Antonio Rubio-Abadal, and Leticia Tarruell. A Strontium Quantum-Gas Microscope. *PRX Quantum*, 5(2):020316, 2024.

[38] Jun Rui, David Wei, Antonio Rubio-Abadal, Simon Hollerith, Johannes Zeiher, Dan M. Stamper-Kurn, Christian Gross, and Immanuel Bloch. A subradiant optical mirror formed by a single structured atomic layer. *Nature*, 583(7816):369–374, 2020.

[39] Kritsana Srakaew, Pascal Weckesser, Simon Hollerith, David Wei, Daniel Adler, Immanuel Bloch, and Johannes Zeiher. A subwavelength atomic array switched by a single Rydberg atom. *Nature Physics*, 19(5):714–719, 2023.

[40] A. Asenjo-Garcia, M. Moreno-Cardoner, A. Albrecht, H. J. Kimble, and D. E. Chang. Exponential improvement in photon storage fidelities using subradiance and "selective radiance" in atomic arrays. *Physical Review X*, 7(3):031024, 2017.

[41] M T Manzoni, M Moreno-Cardoner, A Asenjo-Garcia, J V Porto, A V Gorshkov, and D E Chang. Optimization of photon storage fidelity in ordered atomic arrays. *New Journal of Physics*, 20(8):083048, 2018.

[42] M. Moreno-Cardoner, D. Goncalves, and D. E. Chang. Quantum Nonlinear Optics Based on Two-Dimensional Rydberg Atom Arrays. *Physical Review Letters*, 127(26):263602, 2021.

[43] Daniel Goncalves, Lisa Bombieri, Giovanni Ferioli, Sara Pancaldi, Igor Ferrier-Barbut, Antoine Browaeys, Ephraim Shahmoon, and Darrick E. Chang. Driven-dissipative phase separation in free-space atomic ensembles, 2024.

[44] Loïc Henriet, James S. Douglas, Darrick E. Chang, and Andreas Albrecht. Critical open-system dynamics in a one-dimensional optical-lattice clock. *Physical Review A*, 99(2):023802, 2019.

[45] Hannes Pichler, Tomás Ramos, Andrew J. Daley, and Peter Zoller. Quantum optics of chiral spin networks. *Physical Review A*, 91(4):042116, 2015.

[46] Nadav Antman Ron, Maor Carmi, and Rivka Bekenstein. Atom-Atom entanglement generation via collective states of atomic rings. *Physical Review Research*, 6(4):L042051, 2024.

[47] Martin Hebenstreit, Barbara Kraus, Laurin Ostermann, and Helmut Ritsch. Subradiance via entanglement in atoms with several independent decay channels. *Physical Review Letters*, 118(14):143602, 2017.

[48] A. Asenjo-Garcia, H. J. Kimble, and D. E. Chang. Optical waveguiding by atomic entanglement in multilevel atom arrays. *Proceedings of the National Academy of Sciences*, 116(51):25503–25511, 2019.

[49] Stuart J. Masson, Jacob P. Covey, Sebastian Will, and Ana Asenjo-Garcia. Dicke superradiance in ordered arrays of multilevel atoms. *PRX Quantum*, 5(1):010344, 2024.

[50] Wai-Keong Mok, Stuart J. Masson, Dan M. Stamper-Kurn, Tanya Zelevinsky, and Ana Asenjo-Garcia. Ground-state selection via many-body superradiant decay. *Physical Review Research*, 7(2):L022015, 2025.

[51] A. Piñeiro Orioli and A. M. Rey. Dark states of multilevel fermionic atoms in doubly filled optical lattices. *Physical Review Letters*, 123(22):223601, 2019.

[52] A. Piñeiro Orioli and A. M. Rey. Subradiance of multilevel fermionic atoms in arrays with filling n ≥ 2. *Physical Review A*, 101(4):043816, 2020.

[53] A. Piñeiro Orioli, J. K. Thompson, and A. M. Rey. Emergent dark states from superradiant dynamics in multilevel atoms in a cavity. *Physical Review X*, 12(1):011054, 2022.

[54] Sanaa Agarwal, A. Piñeiro Orioli, J. K. Thompson, and A. M. Rey. Entanglement generation in weakly driven arrays of multilevel atoms via dipolar interactions. *Physical Review Letters*, 133(23):233003, 2024.

[55] B. Olmos, D. Yu, Y. Singh, F. Schreck, K. Bongs, and I. Lesanovsky. Long-range interacting many-body systems with alkaline-earth-metal atoms. *Physical Review Letters*, 110(14):143602, 2013.

[56] W.F. Meggers and J.L. Tech. The first spectrum of ytterbium (yb i). *Journal of Research of the National Bureau of Standards*, 83(1):13, 1978.

[57] S. G. Porsev, Yu. G. Rakhlina, and M. G. Kozlov. Electric-dipole amplitudes, lifetimes, and polarizabilities of the low-lying levels of atomic ytterbium. *Phys. Rev. A*, 60:2781–2785, 1999.

[58] Tommaso Caneva, Marco T. Manzoni, Tao Shi, James S. Douglas, J. Ignacio Cirac, and Darrick E. Chang. Quantum dynamics of propagating photons with strong interactions: A generalized input-output formalism. *New Journal of Physics*, 17(11):113001, 2015.

[59] Heinz-Peter Breuer and Francesco Petruccione. *The Theory of Open Quantum Systems*. Oxford University Press, 2002.

[60] Pedro de Vries, David V. van Coevorden, and Ad Lagendijk. Point scatterers for classical waves. *Rev. Mod. Phys.*, 70:447–466, Apr 1998.

[61] H. J. Lipkin, N. Neshkov, and A. J. Glick. Validity of many-body approximation methods for a solvable model. 1. Exact solutions and perturbation theory. *Nucl. Phys.*, 62:188–198, 1965.

[62] Emi Yukawa, Masahito Ueda, and Kae Nemoto. Classification of spin-nematic squeezing in spin-1 collective atomic systems. *Physical Review A*, 88(3):033629, 2013.

[63] Martin Greiter and Stephan Rachel. Valence bond solids for su(n) spin chains: Exact models, spinon confinement, and the Haldane gap. *Physical Review B*, 75(18):184441, 2007.

[64] G. Vidal and R. F. Werner. Computable measure of entanglement. *Physical Review A*, 65(3):032314, 2002.

[65] Asher Peres. Separability Criterion for Density Matrices. *Physical Review Letters*, 77(8):1413–1415, 1996.

[66] Michał Horodecki, Paweł Horodecki, and Ryszard Horodecki. Separability of mixed states: Necessary and sufficient conditions. *Physics Letters A*, 223(1):1–8, 1996.

[67] Maciej Lewenstein and Anna Sanpera. Separability and Entanglement of Composite Quantum Systems. *Physical Review Letters*, 80(11):2261–2264, 1998.

[68] Meng-Jia Chu, Jun Ren, and Z. D. Wang. Deterministic steady-state subradiance within a single-excitation basis. *npj Quantum Information*, 11(1):99, 2025.

Appendices

A Quantum jump formalism

A.1 Collective jumps

Collective radiance effects are naturally described using collective jump operators instead of single atom lowering and raising operators. Each atom i, has the two possible decay channels: $\hat{\sigma}_i^{g_1 e}$ and $\hat{\sigma}_i^{g_2 e}$. Therefore, the column vector that lists all elementary jumps is of length 2N:

$$\begin{pmatrix} \sigma_1^{g_1 e} \\ \sigma_1^{g_2 e} \\ . \\ . \\ . \\ \sigma_N^{g_1 e} \\ \sigma_N^{g_2 e} \end{pmatrix} \tag{34}$$

To find the collective jumps operators, we define the enlarged dissipative matrix $\Gamma_{ij}^{g_\alpha g_\beta}$:

$$\mathbf{\Gamma} = \begin{pmatrix} \Gamma_{ij}^{g_1 g_1} & \Gamma_{ij}^{g_1 g_2} \\ \Gamma_{ij}^{g_2 g_1} & \Gamma_{ij}^{g_2 g_2} \end{pmatrix}, \tag{35}$$

$\Gamma_{ij}^{g_1 g_1}$ and $\Gamma_{ij}^{g_2 g_2}$ connect the same transition on different atoms. The difference from the two-level case comes from the non-diagonal blocks mixing the different transition channels $\Gamma_{ij}^{g_1 g_2}$ and $\Gamma_{ij}^{g_2 g_1}$ (see Fig. 3). This matrix is diagonalized to obtain eigenvectors $\mathbf{\Gamma}\vec{v}_\nu = \Gamma_\nu \vec{v}_\nu$, for $\nu = 1, ..., 2\text{N}$, allowing to define the collective jump operators as:

$$\hat{\text{O}}_\nu = \sum_{g_\alpha=1}^{2} \sum_{i=1}^{N} v_{i,g_\alpha}^{\nu} \sigma_i^{g_\alpha e}, \tag{36}$$

The adjoint $(\hat{\text{O}}_\nu)^\dagger$ is the corresponding raising operator.

A.2 Quantum jumps algorithm

Once we have obtained the collective jump operators we can write the master equation in the diagonal form for the dissipative part:

$$\dot{\rho} = -\frac{i}{\hbar}\left[\mathcal{H}, \rho\right] + \sum_{\nu}^{2N} \frac{\Gamma_\nu}{2}\left(2\hat{\text{O}}_\nu \rho \hat{\text{O}}_\nu^\dagger - \{\hat{\text{O}}_\nu^\dagger \hat{\text{O}}_\nu, \rho\}\right). \tag{37}$$

Starting with a pure state $\rho(0) = |\psi(0)\rangle\langle\psi(0)|$ and evolving under a small time δt:

$$\rho(\delta t) = (1 - \sum_{\nu=1}^{2N} \delta p_\nu)|\psi_d(\delta t)\rangle\langle\psi_d(\delta t)| + \sum_{\nu=1}^{2N} \delta p_\nu |\psi_\nu^j(\delta t)\rangle\langle\psi_\nu^j(\delta t)|, \tag{38}$$

where the normalized states are:

$$|\psi_d(\delta t)\rangle = \frac{1 - i\mathcal{H}_{\text{eff}}\delta t}{\sqrt{1 - \sum_{\nu=1}^{2N} \delta p_\nu}}|\psi(0)\rangle \tag{39a}$$

$$|\psi_\nu^j(\delta t)\rangle = \frac{\hat{\text{O}}_\nu}{\sqrt{\delta p_\nu / \delta t}}|\psi(0)\rangle. \tag{39b}$$

The effective non-hermitian Hamiltonian and the probability δp_ν are defined as:

$$\mathcal{H}_{\text{eff}} = \mathcal{H} - \frac{i}{2}\sum_{\nu=1}^{2N}\Gamma_\nu \hat{\mathrm{O}}_\nu^\dagger \hat{\mathrm{O}}_\nu, \tag{40a}$$

$$\delta p_\nu = \delta t \langle\psi(0)|\hat{\mathrm{O}}_\nu^\dagger \hat{\mathrm{O}}_\nu|\psi(0)\rangle., \tag{40b}$$

Eq. 38 can be interpreted as following: after δt, ρ becomes a mixed state composed by $|\psi_d(\delta t)\rangle$ (coherent evolution under the non-Hermitian Hamiltonian) with probability $1-\sum_{\nu=1}^{2N}\delta p_\nu$, and any of the 2N states $|\psi_\nu^j(\delta t)\rangle$ given by the jump $|\psi_\nu^j(\delta t)\rangle \propto \hat{\mathrm{O}}_\nu|\psi(0)\rangle$ with probability δp_ν. This defines a strategy for calculating the time evolution of a quantum state:

Quantum jumps algorithm

1. From a given initial state $|\psi(0)\rangle$, compute all the decay probabilities δp_ν.
2. Draw a random number $0 \leq P_{\text{rand}} \leq 1$. If $P_{\text{rand}} > \sum_\nu^{2N}\delta p_\nu$ the state evolves continuously according to equation to Eq. 39a. If $\sum_\nu^k \delta p_\nu < P_{\text{rand}} < \sum_\nu^{k+1}\delta p_\nu$, state jumps to $|\psi_k^j(t+\delta t)\rangle$ with operator $\hat{\mathrm{O}}_k$ (see Fig. 12).

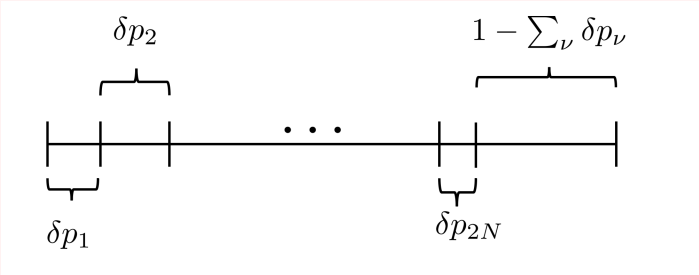

Figure 12: Schematic representation of the quantum jumps algorithm. Probabilities are divided into 2N decay channels with different weights δp_ν. The remaining probability corresponds to the deterministic evolution under the effective non-hermitian Hamiltonian.

3. Repeat steps (1)-(2) until the final time t_{final} is reached.
4. Repeat steps (1)-(3) a sufficient number of trajectories N_{traj} to obtain different quantum trajectories and avarege over them. When N_{traj} is sufficiently large any expectation value of an operator converges to the exact result.

B SU(3) notation

B.1 Gell-Mann matrices

The Gell-Mann definition as generators of SU(3) is:

$$\lambda_1 = \begin{pmatrix} 0 & 1 & 0 \\ 1 & 0 & 0 \\ 0 & 0 & 0 \end{pmatrix}, \quad \lambda_2 = \begin{pmatrix} 0 & -i & 0 \\ i & 0 & 0 \\ 0 & 0 & 0 \end{pmatrix}, \quad \lambda_3 = \begin{pmatrix} 1 & 0 & 0 \\ 0 & -1 & 0 \\ 0 & 0 & 0 \end{pmatrix}, \quad \lambda_4 = \begin{pmatrix} 0 & 0 & 1 \\ 0 & 0 & 0 \\ 1 & 0 & 0 \end{pmatrix},$$

$$\lambda_5 = \begin{pmatrix} 0 & 0 & -i \\ 0 & 0 & 0 \\ i & 0 & 0 \end{pmatrix}, \quad \lambda_6 = \begin{pmatrix} 0 & 0 & 0 \\ 0 & 0 & 1 \\ 0 & 1 & 0 \end{pmatrix}, \quad \lambda_7 = \begin{pmatrix} 0 & 0 & 0 \\ 0 & 0 & -i \\ 0 & i & 0 \end{pmatrix}, \quad \lambda_8 = \frac{1}{\sqrt{3}}\begin{pmatrix} 1 & 0 & 0 \\ 0 & 1 & 0 \\ 0 & 0 & -2 \end{pmatrix}.$$

They obey the following commutation relationship: $[\lambda_i, \lambda_j] = 2if_{ijk}\lambda_k$, where f_{ijk} is known as the structure factor. It is a antisymmetric under the exchange of two indices and the non vanishing values are given by:

f^{ijk}	Value
f^{123}	1
$f^{147} = f^{165} = f^{246} = f^{257} = f^{345} = f^{376}$	$\frac{1}{2}$
$f^{458} = f^{678}$	$\frac{\sqrt{3}}{2}$

Table 1: Non vanishing structure factor f_{ijk}. It is antisymmetric under the exchange of two indices.

B.2 Young tableaux

Young's tableaux rules for coupling many three-level atoms:

1. For each N particle draw a box numbered from left to right.
2. From left to right, put the boxes together such that the numbers assigned to them increase in each row from left to right and in each column from top to bottom.
3. Each tableau represents symmetrization over all boxes in the same row and antisymmetrization over all boxes in the same column. Antisymmetrization over all boxes in the same column implies that there can not be more than three boxes on top of each other.
4. After tensor product, each tableau is now an irreducible representation and can be labeled by their Dynkin coordinates (p, q), where $\mathrm{p} = a_1 - a_2$ and $\mathrm{q} = a_2 - a_3$, where a_i is the number of boxes in the ith row.

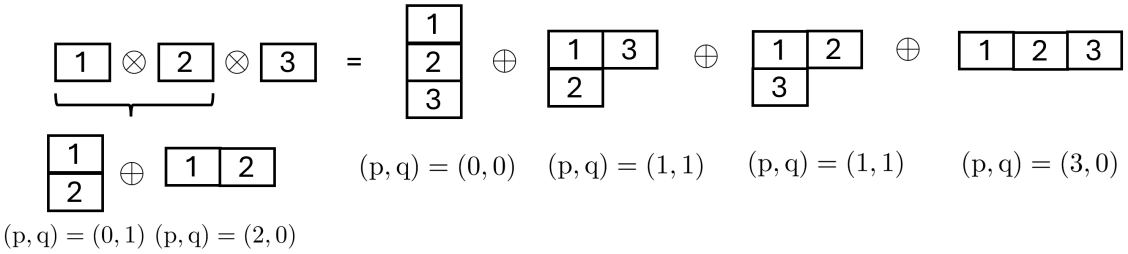

Figure 13: Tensor product of N = 3 three-level particles with Young tableaux.

B.3 N = 6 SU(3) diagrams.

For N = 6, the full set of Dicke decaying diagram for all irreducible representations are shown in Fig. 14.

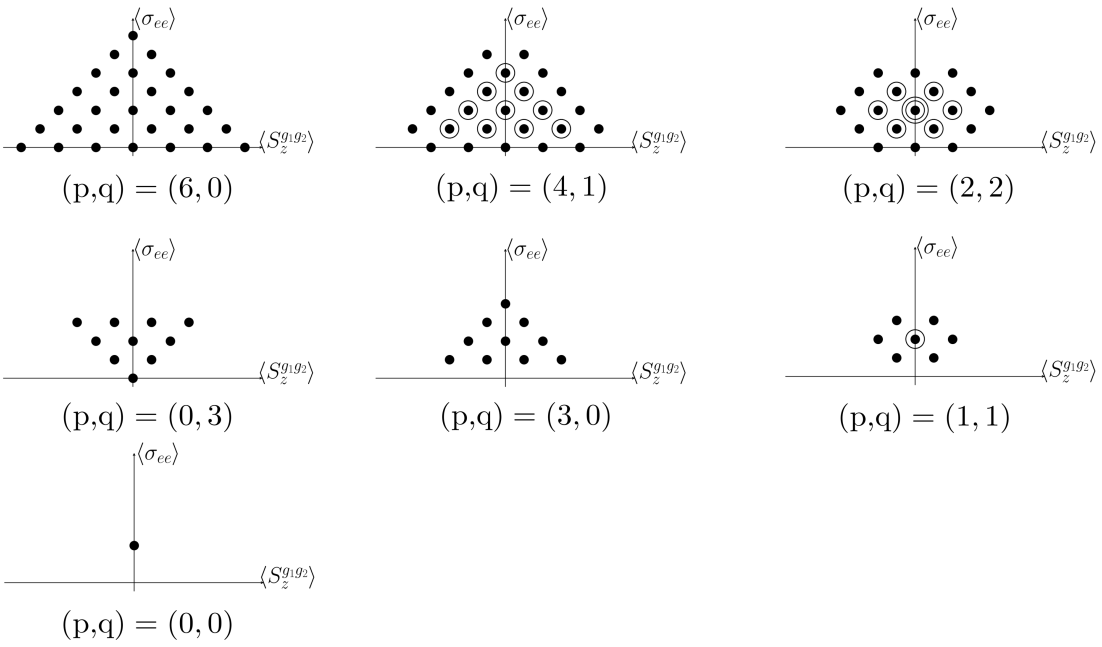

Figure 14: Dicke decaying diagrams for N = 6 Λ-type atoms. One can see seven irreducible representations. Top left panel represents the symmetric subspace $(\mathsf{p},\mathsf{q}) = (6, 0)$ where dynamics happens for an initial $|e\rangle^{\otimes N}$ state (represented by the top point). Degenerate states are represented by the circle around the dot in some representations. Bottom left panel represent the completely antisymmetric subspace (p,q) = (0,0) with just one state, being exactly the subradiant with two excitations.

C Pure states - proof that $E_N(\rho) \geq E_S(\rho)$

We show that $E_N(\rho) \geq E_S(\rho)$ for pure bipartite states, following the discussion in [64]. For a pure state $\rho_{AB} = |\Psi\rangle_{AB}\langle\Psi|$, the Schmidt decomposition is:

$$|\Psi\rangle = \sum_a c_a \, |e'_a\rangle \otimes |e''_a\rangle, \qquad c_a > 0, \quad \sum_a c_a^2 = 1, \tag{41}$$

where c_a are the Schmidt coefficients. Then, the entanglement entropy is

$$E_S(\rho) = -\sum_a c_a^2 \log_2(c_a^2) = 2\sum_a c_a^2 \log_2\Big(\tfrac{1}{c_a}\Big). \tag{42}$$

For pure states, the negativity is given by:

$$\mathcal{N}(\rho) = \tfrac{1}{2}\left[\left(\sum_a c_a\right)^2 - 1\right], \tag{43}$$

and therefore, the logarithmic negativity becomes:

$$E_N(\rho) = \log_2(2\mathcal{N} + 1) = 2\log_2\Big(\sum_a c_a\Big). \tag{44}$$

Now, to compare $E_S(\rho)$ and $E_{\mathcal{N}}(\rho)$, we apply Jensen's inequality. Since $\log(1/x)$ is a convex function for $x > 0$, we have:

$$\sum_a c_a^2 \log_2\left(\tfrac{1}{c_a}\right) \leq \log_2\Big(\sum_a c_a^2 \tfrac{1}{c_a}\Big). \tag{45}$$

Multiplying both sides by 2 this gives:

$$E_S(\rho) = -2\sum_a c_a^2 \log_2\Big(\tfrac{1}{c_a}\Big) \;\leq\; 2\log_2\Big(\sum_a c_a^2 \frac{1}{c_a}\Big). \tag{46}$$

The right-hand side simplifies to:

$$2\log_2\left(\sum_a c_a\right) = E_N(\rho). \tag{47}$$

Thus we have shown $E_{\mathcal{N}}(\rho) \geq E_S(\rho)$. Equality holds when all Schmidt coefficients are equal, which corresponds to maximally entangled states and product states.

D Dissipative dynamics - proof that Dicke model does not mix irreducible representations

To prove that dissipative Dicke dynamics does not mix SU(3) irreducible representations, we show that the Liouvillian superoperator commutes with the quadratic Casimir operator C^2 defined in Eq. 18. Since C^2 charachertized the different irreducible representations with two quantum numbers, (p,q), the condition:

$$\left[C^2, \mathcal{O}\right] = 0 \tag{48}$$

implies that the dynamics preserves each representation sector. The Liouvillian superoperator $\mathcal{O}$ can be written as the sum of the coherent evolution and the jumps: $\mathcal{O} = \mathcal{K} + \mathcal{J}$. Recall that the different terms in the Dicke model can be written as:

$$\mathcal{H}_{\text{eff}} = -i\frac{\Gamma_0}{2}\sum_{ij}(\sigma_i^{eg_1}\sigma_j^{g_1e} + \sigma_i^{eg_2}\sigma_j^{g_2e}) = -i\frac{\Gamma_0}{2}\left(S^{eg_1}S^{g_1e} + S^{eg_2}S^{g_2e}\right), \tag{49a}$$

$$\mathcal{J}[\rho] = \Gamma_0\sum_{ij}\left(\sigma_i^{g_1e}\rho\sigma_j^{eg_1} + \sigma_i^{g_2e}\rho\sigma_j^{eg_2}\right) = \Gamma_0\left(S^{g_1e}\rho S^{eg_1} + S^{g_2e}\rho S^{eg_2}\right), \tag{49b}$$

where $\mathcal{K}[\rho] = -i\left[\mathcal{H}_{\text{eff}}, \rho\right]$. Moreover, the different collective raising and lowering operators are: $\mathrm{S}^{\substack{g_1g_2\\g_2g_1}} = \Lambda_1 \pm i\Lambda_2$, $\mathrm{S}^{\substack{eg_2\\g_2e}} = \Lambda_6 \pm i\Lambda_7$ and $\mathrm{S}^{\substack{eg_1\\g_1e}} = \Lambda_4 \pm i\Lambda_5$, given by the collective Gell-Mann matrices defined before: $\Lambda_a = \sum_{i=1}^{N}\lambda_a(i)$.

We know that the Casimir operator is a group invariant, and therefore it commutes with all group generators: $[C^2, \Lambda_i] = 0\ \forall\ \mathrm{i} = [1, 8]$. As all ladder operators are combinations of Gell-Mann matrices it is also straightforward to see $\left[C^2, \mathrm{S}^{\substack{g_1g_2\\g_2g_1}}\right] = \left[C^2, \mathrm{S}^{\substack{eg_2\\g_2e}}\right] = \left[C^2, \mathrm{S}^{\substack{eg_1\\g_1e}}\right] = 0$. The total commutator can be split in two terms as:

$$\left[C^2, \mathcal{O}\right] = \left[C^2, \mathcal{K}\right] + \left[C^2, \mathcal{J}\right]. \tag{50}$$

The first part of Eq. 50 simplifies to:

$$\begin{aligned}\left[C^2, \mathcal{K}\right] &= -\tfrac{\Gamma_0}{2}\Big(\left[C^2, S^{eg_1}S^{g_1e}\rho\right] + \left[C^2, S^{eg_2}S^{g_2e}\rho\right] \\ &\quad - \left[C^2, \rho S^{eg_1}S^{g_1e}\right] - \left[C^2, \rho S^{eg_2}S^{g_2e}\right]\Big) \\ &= -\tfrac{\Gamma_0}{2}\left(\left[S^{eg_1}S^{g_1e}, \left[C^2, \rho\right]\right] + \left[S^{eg_2}S^{g_2e}, \left[C^2, \rho\right]\right]\right).\end{aligned} \tag{51}$$

The second part of Eq. 50 is:

$$\begin{aligned}\left[C^2, \mathcal{J}\right] &= \Gamma_0\left(\left[C^2, S^{g_1e}\rho S^{eg_1}\right] + \left[C^2, S^{g_2e}\rho S^{eg_2}\right]\right) \\ &= \Gamma_0\Big(S^{g_1e}\rho\left[C^2, S^{eg_1}\right] + S^{g_1e}\left[C^2, \rho\right]S^{eg_1} + \left[C^2, S^{g_1e}\right]\rho S^{eg_1} \\ &\quad + S^{g_2e}\rho\left[C^2, S^{eg_2}\right] + S^{g_2e}\left[C^2, \rho\right]S^{eg_2} + \left[C^2, S^{g_2e}\right]\rho S^{eg_2}\Big) \\ &= \Gamma_0\left(S^{g_1e}\left[C^2, \rho\right]S^{eg_1} + S^{g_2e}\left[C^2, \rho\right]S^{eg_2}\right).\end{aligned} \tag{52}$$

After straightforward algebra (Eqs. 51–52), one arrives at:

$$\begin{aligned}\left[C^2, \mathcal{O}\right] = \Gamma_0 \Big(& S^{g_1 e} \left[C^2, \rho\right] S^{e g_1} + S^{g_2 e} \left[C^2, \rho\right] S^{e g_2} \\ & - \tfrac{1}{2} \left[S^{e g_1} S^{g_1 e}, \left[C^2, \rho\right] \right] - \tfrac{1}{2} \left[S^{e g_2} S^{g_2 e}, \left[C^2, \rho\right] \right] \Big) .\end{aligned} \tag{53}$$

Therefore, in the most general case ρ does not commute with C^2. However, if the initial density matrix $\rho(0)$ belongs to a sector with well defined (p,q): $\left[C^2, \rho(0)\right] = 0$ at $t = 0$, and the relation is preserved for all times. Consequently, $\left[C^2, \mathcal{O}\right] = 0$ holds during the dynamics, proving that different irreducible representations do not mix under Dicke evolution.